CINTAL - Centro de Investigação Tecnológica do Algarve

Universidade do Algarve

Vector Sensor Array Processing and Geoacoustic Inversion with MAKAI'05 Sea Trial Data

B. Jiang

University of Algarve   tel: +351-289800131
Campus da Gambelas   fax: +351-289864258
8005-139 Faro,   cintal@ualg.pt
Portugal   www.ualg.pt/cintal

Work requested by	CINTAL Universidade do Algarve, FCT-Campus da Gambelas, 8005-139, Faro, Portugal Tel/Fax: +351-289864258, cintal@ualg.pt, www.ualg.pt/cintal
Laboratory performing The work	SiPLAB - Signal Processing Laboratory Universidade do Algarve, FCT, Campus de Gambelas, 8005-139, Faro, Portugal Tel: +351-289800949, info@siplab.fct.ualg.pt, www.siplab.fct.ualg.pt
Projects	SENSOCEAN
Title	Vector Sensor Array Processing and Geoacoustic Inversion with MAKAI'05 Sea Trial Data
Authors	B. Jiang
Date	August, 2013
Reference	03/13 - SiPLAB
Number of pages	51 (fifty one)
Abstract	This report presents the vector sensor array (VSA) processing and geoacoustic inversion techniques, the performance analysis and Makai EX 2005 data processing results are given.
Clearance level	UNCLASSIFIED
Distribution list	SiPLAB(1), CINTAL (1)
Total number of copies	2 (two)
Acknowledgements	This work was funded by National Funds through FCT-Foundation for Science and Technology under project: SENSOCEAN (PTDC/EEA ELC/104561/2008). **FCT** Fundação para a Ciência e a Tecnologia MINISTÉRIO DA CIÊNCIA, TECNOLOGIA E ENSINO SUPERIOR

Contents

List of Figures

Abstract

Underwater acoustic vector sensor has received much more attentions in recent a few decades. One type of high precise high-frequency vector sensor TV-001, succeeded for several applications in Makai Ex05 sea trial, such as direction-of-arrival (DOA) estimation, geoacoustic inversion, tomography, MIMO communications. In this report, the vector sensor array (VSA) direction finding performance, including the array directivity index (DI), array gain (AG), and Cramér-Rao bound (CRB) are studied. Besides, the main research was focused on the geoacoustic inversion by using various propagation models. One simple inversion method by comparing the downward and upward beams was studied, i.e. bottom reflection coefficient (BRC) matching method, the results showed that the ($p+v$) processor is the best. The seabed parameter sensitivities were studied, and the compressional velocity was found could be inverted by matched-field inversion (MFI) methods. The CRB's of geoacoustic parameter estimates are derived, which also demonstrated that the ($p+v$) processing outperforms others. A two-step inversion method was proposed. First, the compressional velocity, along with the receiver range and depth were optimized using genetic algorithm (GA). Secondly, the optimized range and depth information was fed back to improve the accuracy of the replica fields, then the compressional velocity dependent replicas were matched with the real data, giving high resolution and precise results during the period of nearly two hours.

Chapter 1

Introduction

Geoacoustic inversion plays an important role in underwater acoustics. It is to characterize the ocean bottom by estimating some key parameters such as the compressional and shear wave velocities and their attenuations, sediment layers and thicknesses, densities, etc. Traditionally, low frequency full-field geoacoustic inversions were employed, the problem is that a high source level transducer and large aperture receiving hydrophone array are needed. However, when using high frequency inversion methods, it allows the array length to be substantially shortened and suffers from much less shipping interference. If the array lengths can be reduced to about 1 m then it might be hull-mounted or towed from a surface ship or submerged vehicle (e.g. an autonomous underwater vehicle, AUV). Vector sensor can measure both the pressure and the particle velocity components, so it has the ability to estimate the horizontal azimuths and vertical elevation angles. Combining with vector field might improve the geoacoustic inversion performance. This report further investigates whether there are advantages of using VSA in signal processing and geoacoustic inversion applications, through theoretical analysis and Makai Ex05 sea trial data processing.

This report is organized as follows: Chapter 2 introduces the VSA beamforming techniques, gives the expressions of directivity index (DI) and array gain (AG) for some processing methods, and the CRB performance of bearing estimates is analyzed. Chaper 3 derives the bottom reflection coefficient (BRC) inversion method, introduces the Makai Ex05 sea trial briefly, and gives the seabed parameter inversion results. Chapter 4 describes the Bartlett sensitivity analysis of the seabed parameters based on various acoustic models, and the CRB's of seabed parameters are given. Chapter 5 describes the genetic inversion method and a proposed two-step inversion method, and gives a compressional velocity-time record (CpTR), showing the greatly improved performance. Chapter 6 concludes this report and gives some potentially meaningful further work.

Chapter 2

Vector Sensor Array Processing

The vector sensor array (VSA) is illustrated in Figure 2.1, the VSA with inter-element spacing d is located on the z axis downwards, the elevation and azimuth angle of the incoming signal are denoted as ϕ and θ, then the array output signal vector can be written as
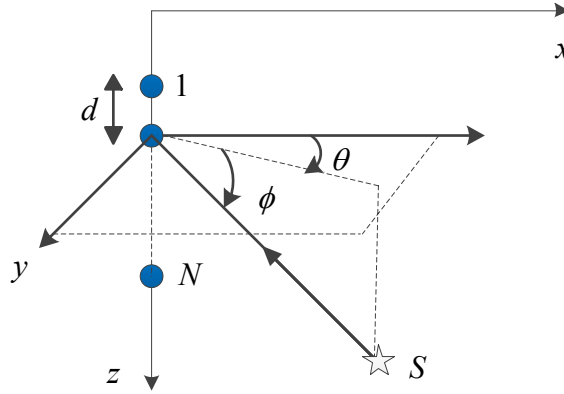
Figure 2.1: VSA geometrical illustration.

$$x = As(t) + n(t) \tag{2.1}$$

where,

$$x = [p_1, v_{1x}, v_{2x}, v_{1z}, \cdots, p_N, v_{Nx}, v_{Ny}, v_{Nz}]^T \tag{2.2}$$

v is the particle velocity, and the velocities are related to acoustic pressure by Euler's equation [2]:

$$\bar{v} = -\frac{j}{\rho\omega}\nabla p \tag{2.3}$$

where ρ is the medium density, and ω the signal angular frequency. The steering matrix A is:

$$A = a_p(\phi) \otimes h(\theta, \phi) \tag{2.4}$$

where $\otimes$ denotes the Kronecker product, and

$$\boldsymbol{a}_p(\phi) = [1, e^{j2\pi f d\sin\phi/c}, \cdots, e^{j2\pi f(N-1)d\sin\phi/c}]^T \tag{2.5}$$

is the steering vector of the equivalent pressure sensor array, and $\boldsymbol{h}$ is the response of a single vector sensor at the origin [3]:

$$\boldsymbol{h}(\theta,\phi) = [1, \boldsymbol{u}(\theta,\phi)]^T \tag{2.6}$$

where

$$\boldsymbol{u}(\theta,\phi) = [\cos\phi\cos\theta, \cos\phi\sin\theta, \sin\phi]^T \tag{2.7}$$

is the source direction vector, i.e., a unit-norm vector pointing from the origin toward the source.

$\boldsymbol{a}_p$ contains the time delay information between sensors, $\boldsymbol{u}$ accounts for the directional response of each vector sensor, when the orientations of all the sensors are in line, then $\boldsymbol{u}$ is independent of the sensor locations

2.1   VSA Beamforming

The VSA beamforming may include the p-only, ($p+v$), v-only, v_r-only, v_z-only, v_x, v_y processors, etc. ($p+v$) refers to using the pressure and all the three velocity components, and v-only is that only the three velocities are used. After having estimated the array sample correlation matrix, the conventional beamforming (CBF, also named as Bartlett beamforming) and the high resolution methods such as MVDR, MUSIC can be utilized. The resolution and interference suppression capability can be improved by using MVDR.

The array sample correlation matrix is:

$$\hat{\boldsymbol{R}} = \frac{1}{N_{\text{snaps}}}\sum_l \boldsymbol{x}(l)\boldsymbol{x}^H(l) \tag{2.8}$$

where N_{snaps} is the number of snapshots.

To select the pressure and particle components to be used, five selection matrices are defined:

$$\boldsymbol{T}_p = \boldsymbol{I}_N \otimes [1\,0\,0\,0] \tag{2.9}$$

$$\boldsymbol{T}_{p+v} = \boldsymbol{I}_{4N} \tag{2.10}$$

$$\boldsymbol{T}_v = \boldsymbol{I}_N \otimes [[1\,0\,0\,0]^T\ \boldsymbol{I}_3] \tag{2.11}$$

$$\boldsymbol{T}_{v_z} = \boldsymbol{I}_N \otimes [0\,0\,0\,1] \tag{2.12}$$

$$\boldsymbol{T}_{v_r} = \boldsymbol{I}_M \otimes [[0\,0]^T\ \boldsymbol{I}_2\ [0\,0]^T] \tag{2.13}$$

where $\boldsymbol{I}$ is the unit matrix with the subscript representing its dimension size.

For different processors, the resulting correlation matrix can be written as

$$\hat{R}_{\text{proc}} = T_{\text{proc}}^{T} \hat{R} T_{\text{proc}} \tag{2.14}$$

and the transformed steering vector is

$$a_{\text{proc}} = T_{\text{proc}}^{T} a \tag{2.15}$$

Then, the spatial spectra of CBF and MVDR can be written as

$$P_{\text{CBF}} = a_{\text{proc}}^{T} \hat{R}_{\text{proc}} a_{\text{proc}} \tag{2.16}$$

$$P_{\text{MV}} = 1 / (a_{\text{proc}}^{T} \hat{R}_{\text{proc}}^{-1} a_{\text{proc}}) \tag{2.17}$$

Some other VSA data models and performance analyses can be found in [4], [5].

2.2   Directivity Index (DI)

Directivity index DI is a measure of the directionality of the projectors or hydrophone receivers. It is used to describe the ability of suppressing spatial isotropic noise. DI is defined as [6]:

$$\text{DI} = \frac{4\pi D(\theta_0, \phi_0)}{\int_0^{2\pi} \int_0^{\pi} D(\theta, \phi) \cos\phi \, d\phi \, d\theta} \tag{2.18}$$

where $D(\theta, \phi)$ is the directionality function.

Some of the DI's of a single vector sensor can be derived and deduced as [7]:

$$\text{DI}_{p-\text{only}} = 1 \tag{2.19}$$

$$\text{DI}_{v_x} = 3\cos\theta_0^2 \cos\phi_0^2 \tag{2.20}$$

$$\text{DI}_{v_y} = 3\sin\theta_0^2 \cos\phi_0^2 \tag{2.21}$$

$$\text{DI}_{v_r-\text{only}} = 3\cos\phi_0^2 \tag{2.22}$$

$$\text{DI}_{v_z-\text{only}} = 3\sin\phi_0^2 \tag{2.23}$$

$$\text{DI}_{(p+v)} = 4 \tag{2.24}$$

$$\text{DI}_{(p+v_r)} = 1 + 3\cos\phi_0^2 \tag{2.25}$$

From (2.19) to (2.25), we can see that, the directivity of vector sensor is azimuth and elevation angles dependent. For p-only processor, it is obviously there is no directivity, the maxima of DI's using only v_x and v_y are $10\lg(3) \approx 4.77$dB, which depend on the azimuth and elevation angle. Also v_r-only and v_z-only processors achieve the maximum DI of 4.77dB in horizontal and vertical plane, respectively. $(p+v)$ processor has the optimal 6dB towards all spatial positions with the proper weight on each component.

The DI's of a VSA can be derived for large N, sometimes using the stationary phase

method, e.g., the DI of VSA v_y processor is [7]:

$$\text{DI}_{v_y}^{\text{VSA}} = \frac{2\cos^2\phi_0 \left(\sum_{n=1}^{N} w_{yn}\right)^2}{\sum_{n=1}^{N} (w_{yn})^2} \tag{2.26}$$

As N increases, and for azimuth $\theta_0=90°$, the DI of a velocity sensor array approaches a gain that is 3dB greater than that of a pressure array. However, from the simulation results in [7], for azimuth $\theta_0=0°$, the DI of v_x processor is a little lower than that of a v_y processor at $\theta_0=90°$.

2.3   Array Gain

DI is limited to ideal isotropic noise, when the noise is spatially inhomogeneous, or there are point interferer sources, array gain (AG) is another measure to assess the array performance. AG is defined as the beamforming output signal-to-noise ratio (SNR) to the input SNR on a single sensor, i.e., the SNR improvement after proper spatial processing.

The optimal array gain can be derived with regard to the noise covariance matrix [6]:

$$\text{AG} = \boldsymbol{a}^H(\theta_0,\phi_0)\boldsymbol{R}_n^{-1}\boldsymbol{a}(\theta_0,\phi_0) \tag{2.27}$$

where $\boldsymbol{R}_n$ is the noise covariance matrix, $\boldsymbol{a}$ is the steering vector.

2.4   Bearing Estimation Performance

Cramér-Rao bound (CRB) is utilized to analyze the bearing estimation performance. For single-source condition, and the noise is assumed to be independent, identically distributed (i.i.d.), zero-mean complex Gaussian processes. With some arithmetic manipulations using results of [4]-[5], the CRB for VSA can be derived as:

$$\text{CRB}_p(\phi) = \frac{1}{2N_{\text{snaps}}} \frac{1}{M\alpha} \left(1 + \frac{1}{M\alpha}\right) J^{-1} \tag{2.28}$$

$$\text{CRB}_v = \frac{1}{2N_{\text{snaps}}} \frac{1}{M\alpha\alpha_I} \left(1 + \frac{1}{M\alpha\alpha_I}\right) \boldsymbol{K}^{-1} \tag{2.29}$$

where, N_{snaps} is the number of snapshots, α is the SNR of the pressure channel, and α_I is the effective increase in SNR, as following:

$$\alpha = \sigma_s^2 / \sigma_{n,p}^2 \tag{2.30}$$

$$\alpha_I = 1 + 1/\eta, \eta = \sigma_{n,v}^2 / \sigma_{n,p}^2 \tag{2.31}$$

η is the noise power ratio between the particle velocity sensor and pressure sensor. And the scalar and the matrix $\boldsymbol{K}$ are given by:

$$J = \frac{\pi^2 (M^2 - 1) d^2 \cos^2 \phi}{3\lambda^2} \tag{2.32}$$

$$K = \begin{bmatrix} (1+\eta)^{-1} \cos^2 \phi & 0 \\ 0 & (1+\eta)^{-1} + J \end{bmatrix} \tag{2.33}$$

Form (2.28), (2.29), it can be seen that, the CRB expression of vector array differs from that of the pressure sensor array in two ways, it contains extra factors of α_I and an additive term K, both of which reduce the CRB of vector array [5]. Due to the additional velocity measurements, the SNR of vector sensor is improved, resulting α_I. K results from direct measurement of the DOA information contained in the velocity field, due to the directivity of each vector sensor.

Figure 2.2 depicts the CRB performance for a 4-element VSA with spacing 10cm, and the signal frequency is 8250Hz, which is one of the tonal frequencies in Makai sea trial, close to the half-wavelength spacing condition. It's obvious that the bearing estimation accuracy is improved by (*p+v*) processing method.

<center>(a)   (b)</center>
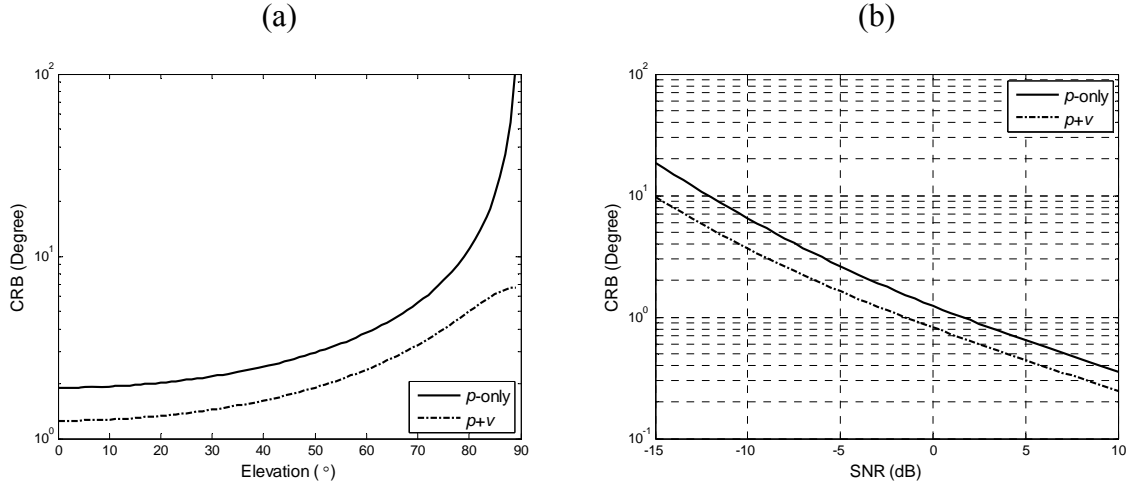
Figure 2.2: CRB performance vs. elevation angle (a) and vs. SNR (b).

Chapter 3

Geoacoustic Inversion by Bottom Reflection Coefficient

In [8], Harrison proposed a method which uses the vertical array measurements to obtain the bottom reflection coefficient (BRC) by comparing the upward with the downward-going noise. This simple ratio is, in fact, the power reflection coefficient, as a function of angle and frequency. Thus, modeling and searching are minimized, and it does not require a detailed environmental knowledge of the noise source distribution. Moreover, this approach can handle multi-layered seabed and is robust to range –dependent environment. So, reflection energy ratio can be extended for small aperture VSA geoacoustic inversion [3]. Figure 3.1 depicts the geometrical principle. The upward incident angle is positive and the downward incident angle is let negative.
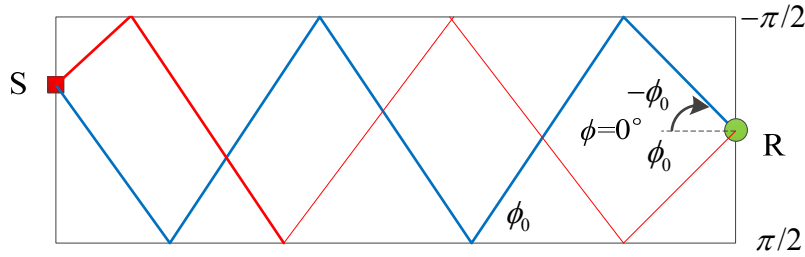
Figure 3.1: Ray approach geometry of a plane wave with vertical arriving angle ϕ_0.

Since a shallow transmitting source is used in Figure 3.1, the SNR is improved, it is expected that the performance of BRC inversion method might be improved, comparing to those using ambient noise such as in [8].

Plane wave beamforming is used to obtain the vertical beam spectra in elevation ϕ's at the source azimuth θ_0. Then, the ratio between downward and upward beam powers is an approximation to the bottom reflection coefficient R_b:

$$R_b[\phi_b(\phi_0)] = \frac{B(-\phi_0)}{B(+\phi_0)} \tag{3.1}$$

where the angle measured by beamforming, ϕ_0 is corrected to the angle at the seabed, ϕ_b, according to the Snell's law:

$$\phi_b = \mathrm{acos}[(c_b / c_r)\cos\phi_0] \tag{3.2}$$

where c_b and c_r are the sound speed at the bottom and at the receiver, respectively.

When the BRC is transformed to dB, it is the bottom reflection loss (BRL).

If there is a sound speed higher than at the receiver depth anywhere above the receiver, denoted as c_m, there is a possibility of a "noise notch", where is surface-noise free [8]. The edge of this range obviously corresponds to a nonzero angle at the receiver:

$$\phi_m = \mathrm{acos}(c_m / c_r) \tag{3.3}$$

3.1 Ray-based Bottom Reflection Derivation

To illustrate the BRC method more straightforwardly, the ray based derivation is presented considering an iso-speed water column.

The sound field at angular frequency ω can be calculated from ray amplitudes and arrivals at a receiver depth z, as follows [9]:

$$p(\omega, r, z) = \sum_{m=1}^{M} A_m e^{j\omega\tau_m} \tag{3.4}$$

where A_m is the mth arrival amplitude, and τ_m is the corresponding time delay. The signal cross-spectral density (CSD) function between two vertically separated sensors at depth z_1 and z_2 is:

$$S_\omega(z_1, z_2) = \int_0^{2\pi} \int_0^\infty p(z_1)p^*(z_2)g^2(\phi)r\,dr\,d\theta \tag{3.5}$$

where $g(\phi)$ is a source directivity function, θ is azimuth. Consider the source is omnidirectional, and assume the azimuthal symmetry, then (3.5) can be written as:

$$S_\omega(z_1, z_2) \approx 2\pi \int_0^\infty \sum_m |A_m|^2 \, e^{jk(z_2 - z_1)\sin\phi} r\,dr \tag{3.6}$$

The ray amplitude can be written as [9]:

$$|A_m|^2 = \frac{\cos\phi}{r\,|(dr/d\phi)\sin\phi|}QP_m \tag{3.7}$$

where Q and P_m are related to the volume and boundary losses. Reflecting from the surface suffers the volume loss as $Q = e^{-\beta s_p}$, where s_p is the ray partial cycle distance. For a surface-bottom path, the bottom interaction loss is $e^{-\beta(s_c - s_p)}R_b$, where R_b is the bottom reflection loss, s_c is the complete ray cycle distance. Thus, after a number of surface and bottom reflections, for the downward rays, the loss is:

$$\mathrm{Loss}_{-\pi/2 \to 0} = e^{-\beta s_p}\{1 + R_b e^{-\beta s_c} + (R_b e^{-\beta s_c})^2 + \cdots\} = e^{-\beta s_p}\frac{1}{1 - R_b e^{-\beta s_c}} \tag{3.8}$$

and for the upward rays is:

$$\text{Loss}_{0 \to \pi/2} = e^{-\beta(s_c - s_p)} \{1 + R_b e^{-\beta s_c} + (R_b e^{-\beta s_c})^2 + \cdots\} = e^{-\beta(s_c - s_p)} R_b \frac{1}{1 - R_b e^{-\beta s_c}} \quad (3.9)$$

Combing these losses, (3.6) can be written as:

$$S_\omega(z_1, z_2) = 2\pi \int_0^{\pi/2} \frac{\cot\phi}{1 - R_b e^{\beta s_c}} \{e^{jk(z_2 - z_1)\sin\phi} + R_b e^{-jk(z_2 - z_1)\sin\phi}\} d\phi \quad (3.10)$$

where the small partial cycle distance volume attenuation terms have been suppressed. From (3.10), there are two plane waves with one travelling downward and the other upward, these differ by exactly a scalar R_b, i.e., the power reflection coefficient. So, the BRC inversion method is proven to be effective.

3.2   Makai Ex05 Sea Trial

The Makai experiment took place from 15 Sep to 2 Oct 2005, near the coast of Kauai, Hawai. MakaiEx'05 was the third experiment for high frequency ocean acoustic research, which involves high-resolution tomography, high frequency propagation modeling and acoustic communications. It was organized by HLS and sponsored by ONR, involved a large number of teams both from government and international labs, universities and private companies, such as HLS, UALg, UDEL, SPAWAR, NRL, NURC [1]. The selected area for the Makai Ex05 sea trial is shown in Figure 3.2, and the detailed description can be found in the Makai'05 reports.

This report mainly focuses on VSA geoacoustic inversion algorithms and sea trail data processing. Figure 3.3 shows on the left the vector sensor type TV-001, made by Wilcoxin Corp. with one pressure sensor and three accelerometers arranged in a triaxial configuration, and mounted in a neutrally buoyant package approximately 3.81cm in diameter and 6.35cm long, as on the right in Figure 3.3. Figure 3.4 depicts the average sound speed profile (SSP) during Julian Day 264.
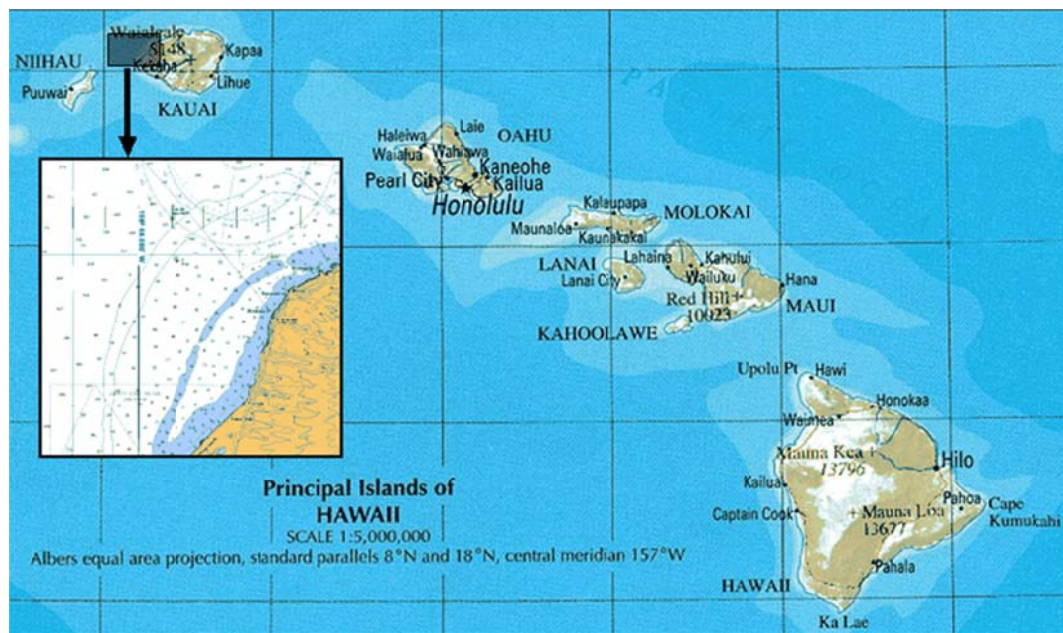
Figure 3.2: Makai experiment site off the northwest coast of Kauai I., Hawaii, USA.
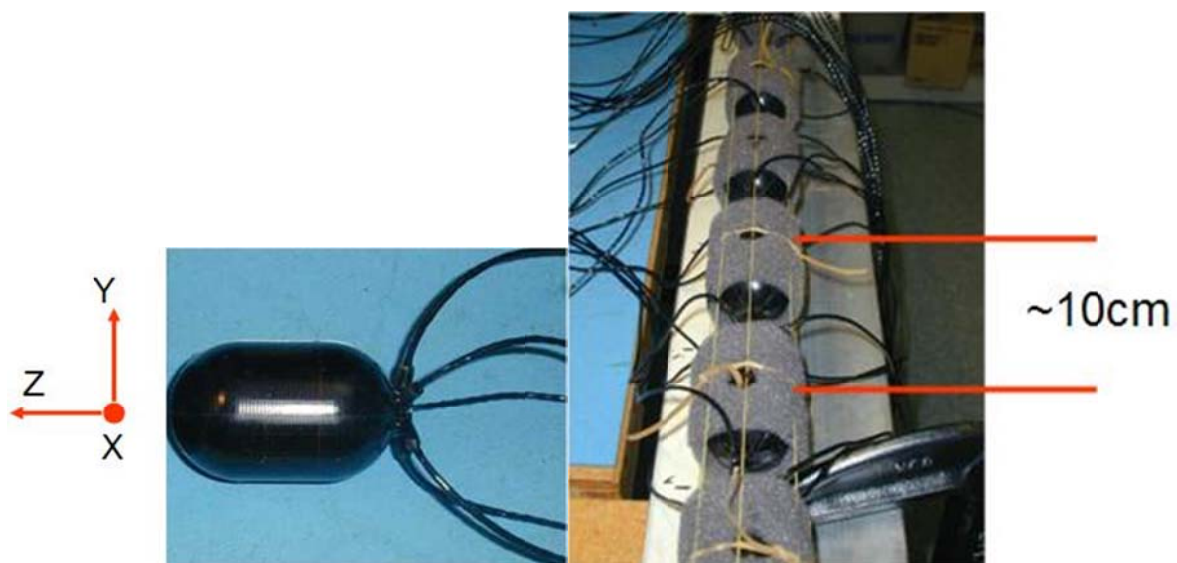
Figure 3.3: TV-001 vector sensor and vector sensor array.
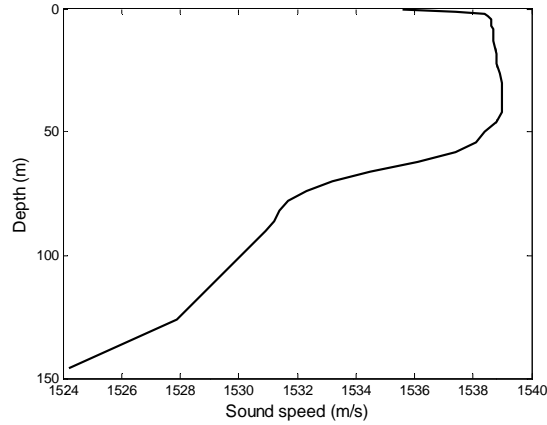
Figure 3.4: Average SSP during Julian Day 264.

3.3 JD268 Data Results

The experimental configuration in Julian Day 268 is illustrated in Figure 3.5. The source is Lubell 916C3, towed from RHIB and deployed at 10m depth, and the receiving VSA was at about 40m depth. For ranges smaller than 500m, the water depth was approximately from 120m, at the source position, to 104m at the receiver. The signal analyzed were the 6s LFM groups in the first region of the field calibration (FC) phase [1]. The environment can be approximated as range-independent, or more precisely, we can use a range-dependent model to get more precise inversion results.
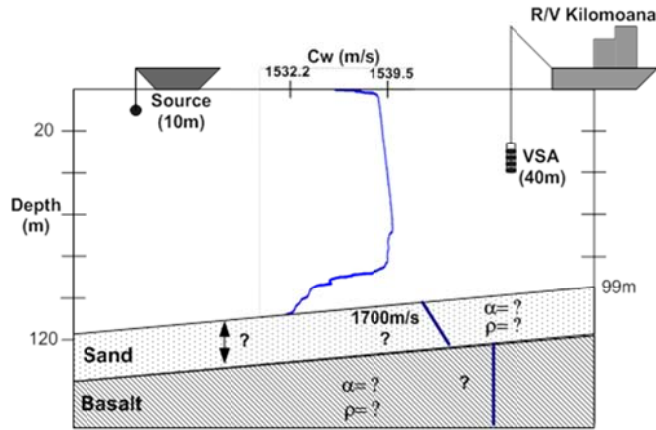
Figure 3.5: Configuration for geoacoustic inversion experiment.

3.3.1 Results at Minute-38

At minute 38, the source-receiver range is about 500m, and the source azimuth is about 43°. From Figure 3.6 to Figure 3.10, some of the processing results are shown by p-only, ($p+v$), v-only, v_z-only and v_r-only processor, respectively. It can be seen that the ($p+v$) method can resolve the azimuthal ambiguity, and the bottom reflection loss is best estimated

among these processors. The v_r-only processor loses one fringe. The resolution and sidelobe performance of v-only processing is a little worse than those of ($p+v$) processing.

(a)   (b)

Figure 3.6: p-only processing results of LFM-min38 data: vertical beam at source azimuth (a) and bottom reflection loss vs. bottom angle (b).

(a)   (b)

(c)

Figure 3.7: (p+v) processing results of LFM-min38 data: 2-D beam response (a), vertical beam at source azimuth (b) and bottom reflection loss vs. bottom angle (c).

20

Figure 3.8: v-only results of LFM-min38 data: 2-D beam response (a), vertical beam at source azimuth (b), ratio of downward-to-upward beam (c) and bottom reflection loss vs. bottom angle (d).

Figure 3.9: v$_z$-only processing results of LFM-min38 data: vertical beam at source azimuth (a) and bottom reflection loss vs. bottom angle (b).

Figure 3.10: v_r-only processing results of LFM-min38 data: vertical beam at source azimuth (a) and bottom reflection loss vs. bottom angle (b).

3.3.2 Results at Minute-48

At minute 48, the source-receiver range is about 300m, Figure 3.11~Figure 3.15 show the corresponding results of *p*-only, (*p+v*), *v*-only, v_z-only and v_r-only processors. In this data set, a new fringe is appeared, from which the critical angle can be inferred. The v_z-only processing shows the worst performance. The fringe in steeper bottom angle area is not clear for v_r-only processing, because no vertical information was used. Consequently, the v_z-component is useful in bottom reflection coefficient estimation, although v_z-only processing can't provide satisfied BRC result. If all of the vector sensors work normally, and the orientations can be adjusted correctly, the (*p+v*) processing is optimal in the BRC inversion method.

(a) (b)
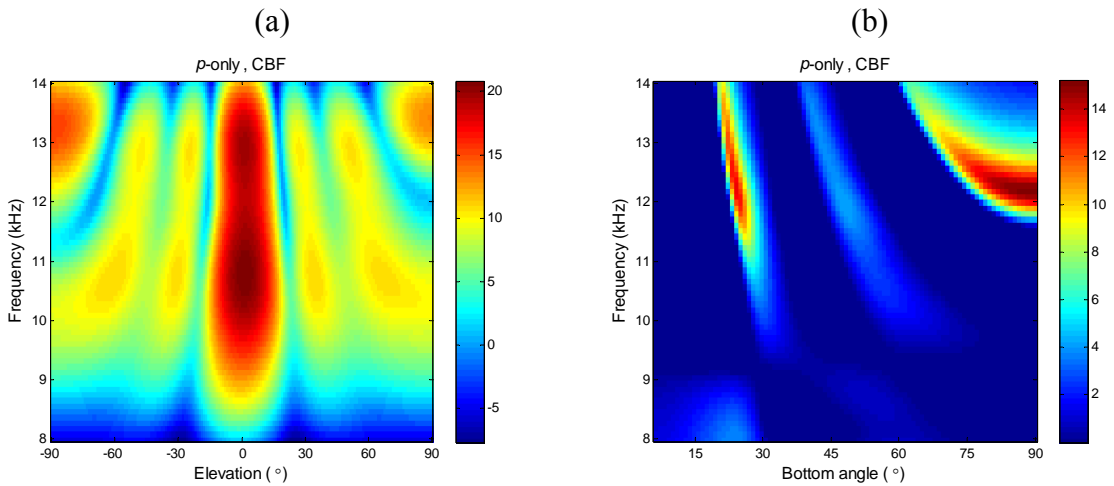
Figure 3.11: p-only processing results of LFM-min48 data: vertical beam at source azimuth (a) and bottom reflection loss vs. bottom angle (b).

(a)

p+v , CBF

(b)

p+v , CBF
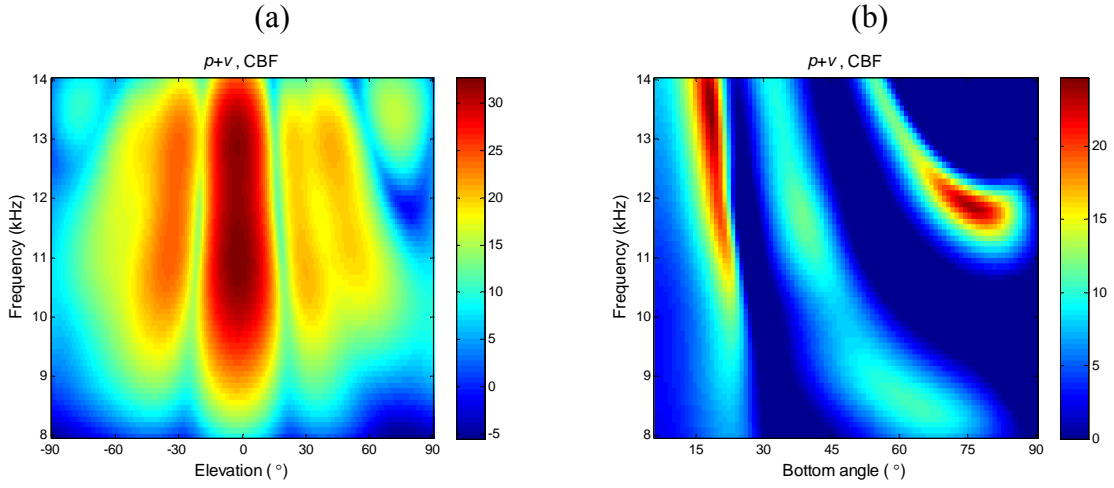
Figure 3.12: (p+v) processing results of LFM-min48 data: vertical beam at source azimuth (a) and bottom reflection loss vs. bottom angle (b).

(a)

v-only , CBF

(b)

v-only , CBF
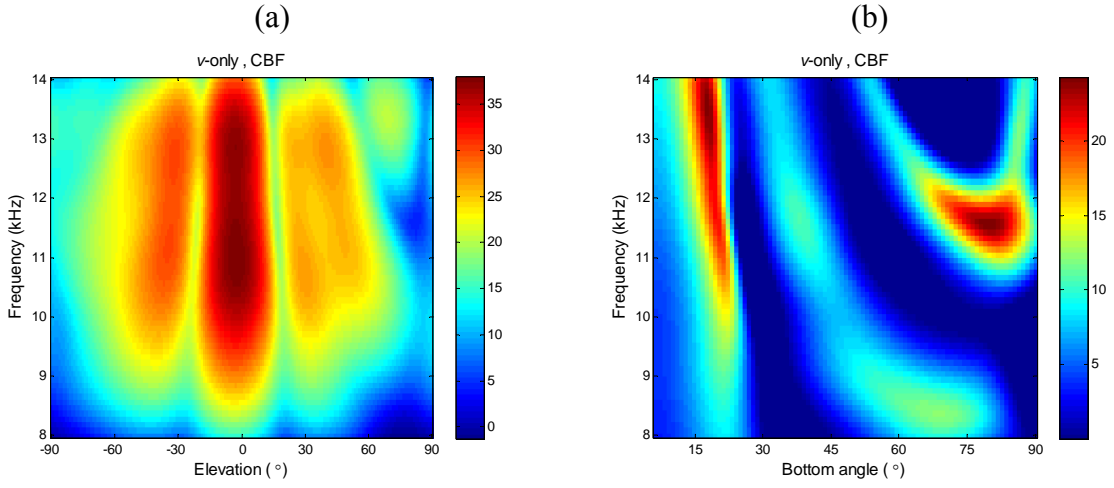
Figure 3.13: v-only processing results of LFM-min48 data: vertical beam at source azimuth (a) and bottom reflection loss vs. bottom angle (b).
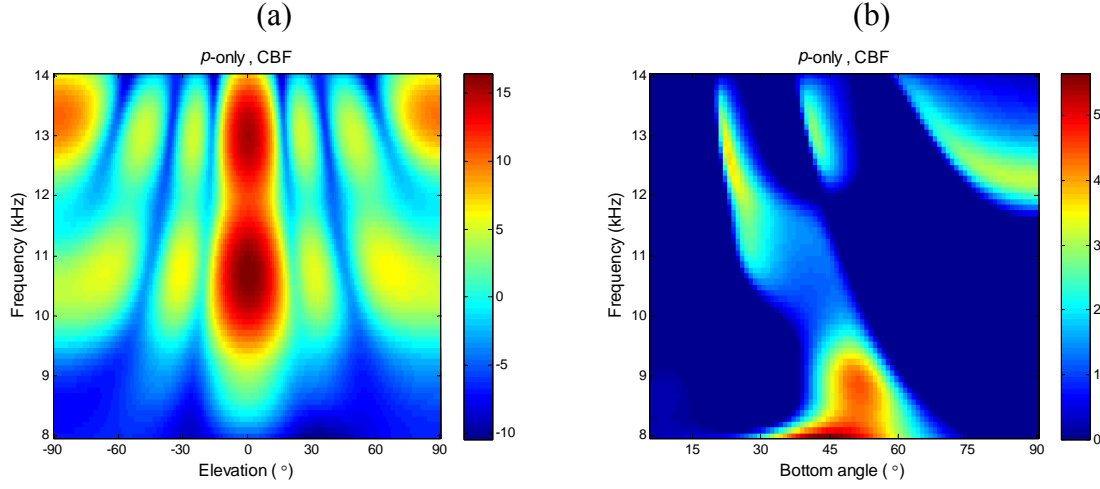

(a)

v_z-only , CBF

(b)

v_z-only , CBF
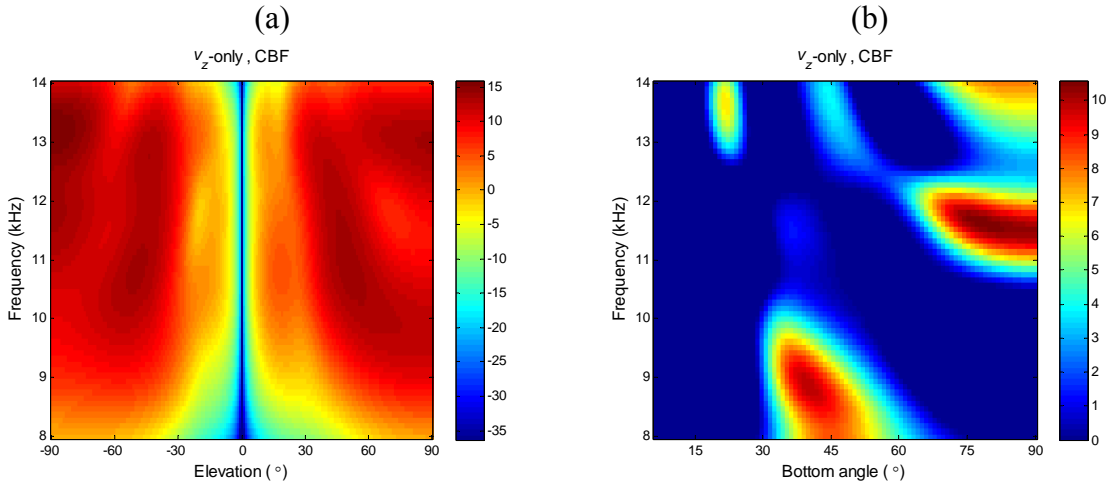
Figure 3.14: v_z-only processing results of LFM-min48 data: vertical beam at source azimuth (a) and bottom reflection loss vs. bottom angle (b).
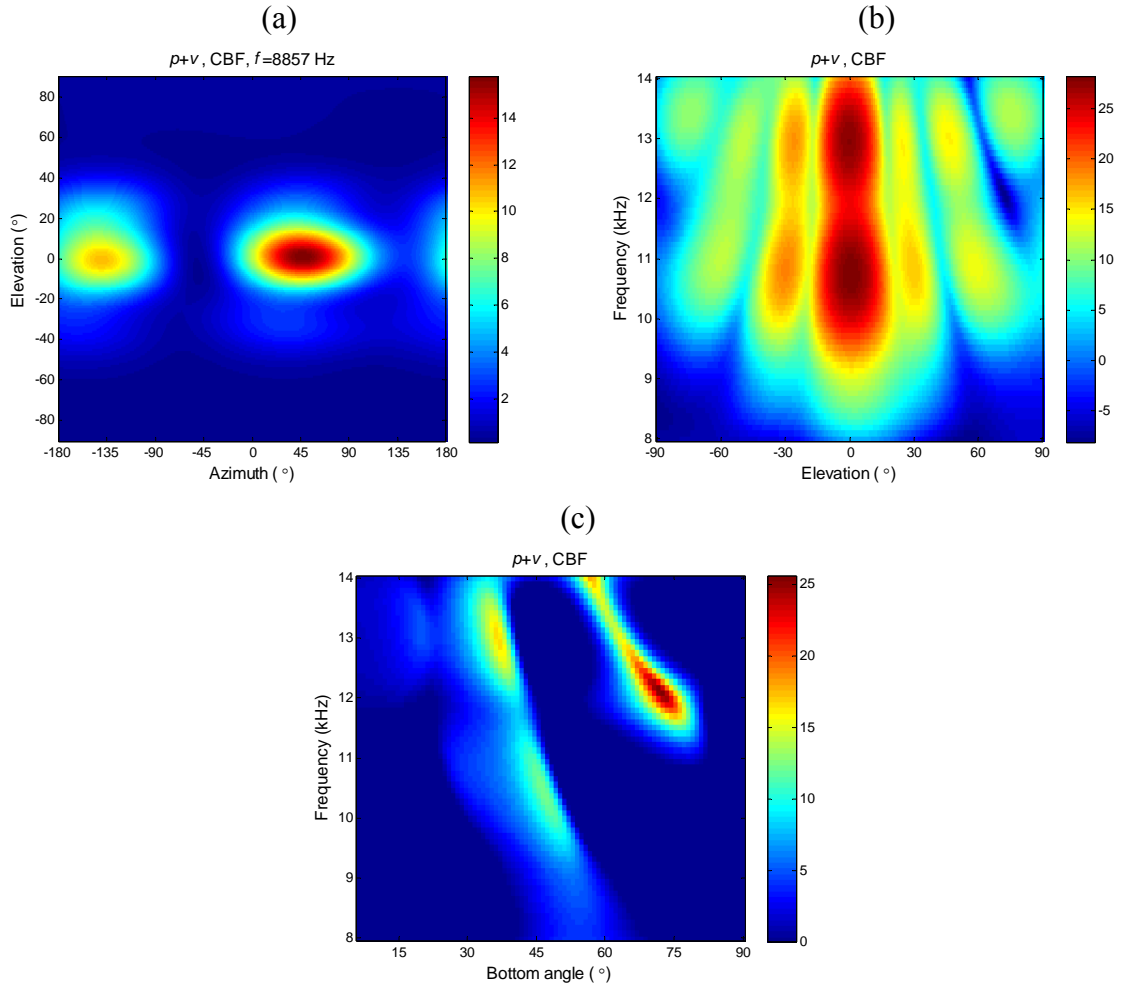
23

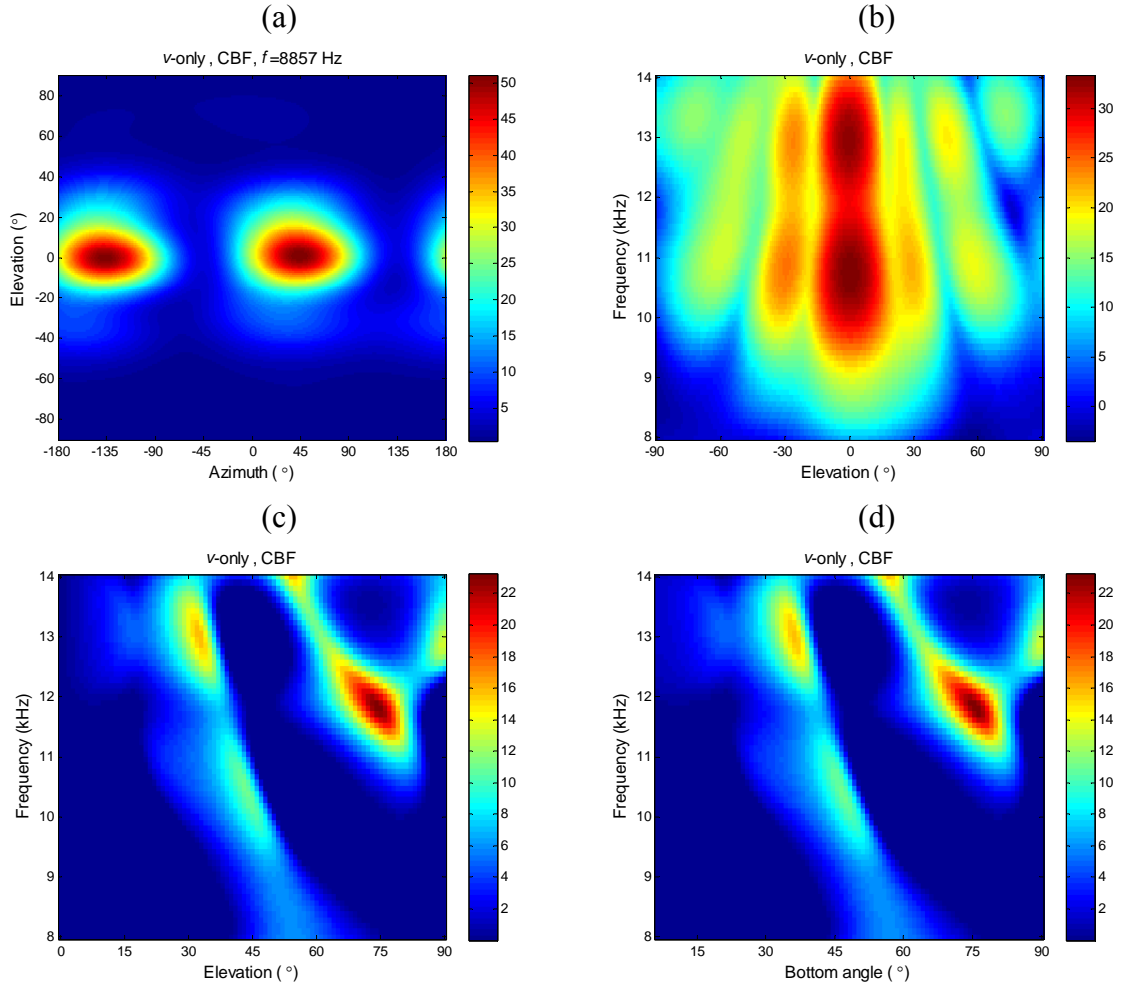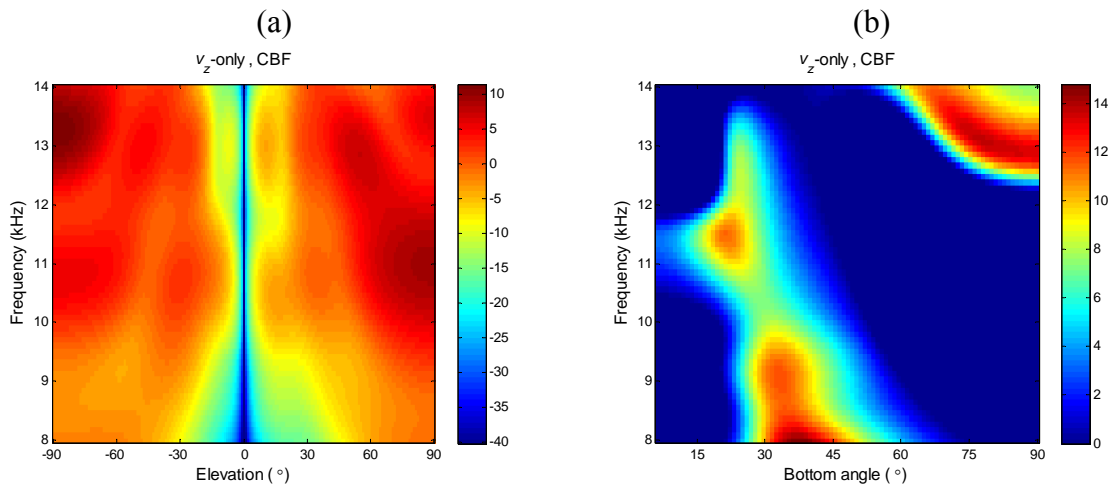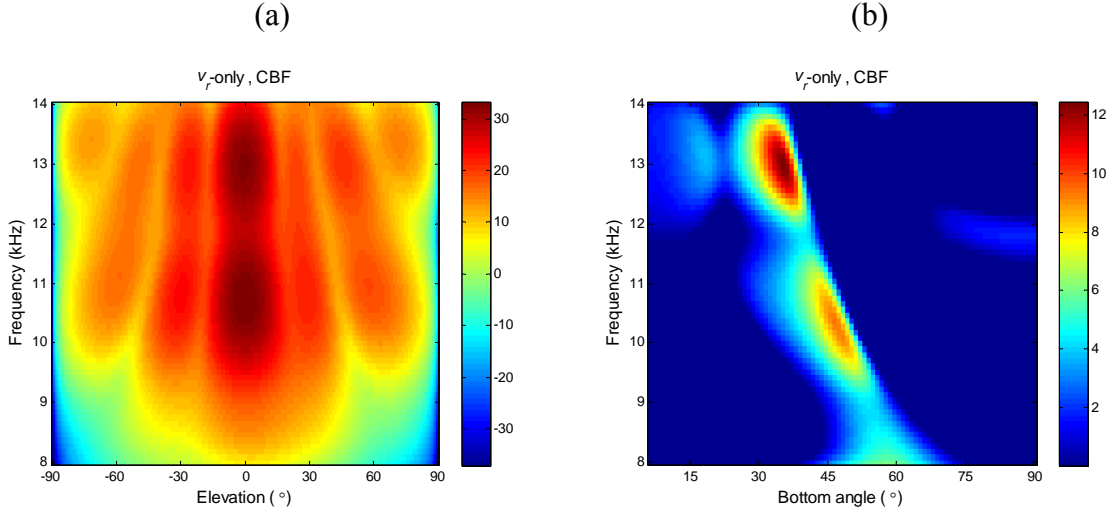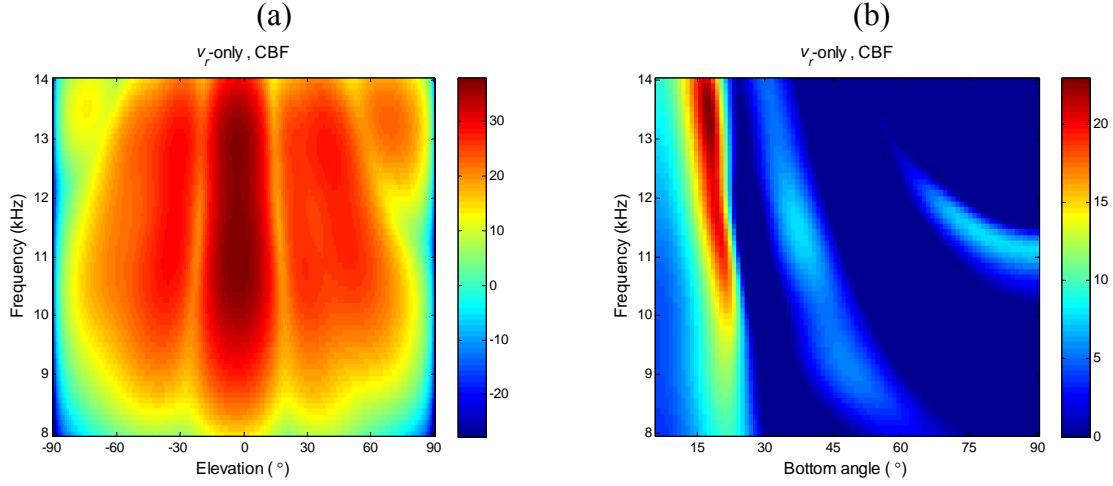*Figure 3.15: v_r-only processing results of LFM-min48 vertical beam at source azimuth (a) and bottom reflection loss vs. bottom angle (b).*

3.3.3 Modeled Bottom Reflection Loss

To estimate the seabed parameters from the BRL results in 3.3.1 and 3.3.2, modeled results are obtained by manually adjusting the model parameters.

Figure 3.16 depicts the bottom reflection loss (BRL) with a two sediment layers model using acoustic toolbox [10], in which the "Bounce" function was utilized. The corresponding parameters used are as in Table 3.1. Three fringes due to the interface reflected signal interference can be seen obviously. Figure 3.17 gives a one sediment layer model result, and the parameters are in Table 3.2. In [1] and [3], SAFARI package was used, and the BRL results are similar to Figure 3.16. SAFARI is more suitable to model the reflection coefficients since it is a more precise seismo-acoustic model, the upgraded SAFARI code, i.e. OASES [11] will be utilized in the future research, since OASES provides improved numerical efficiency and stability.
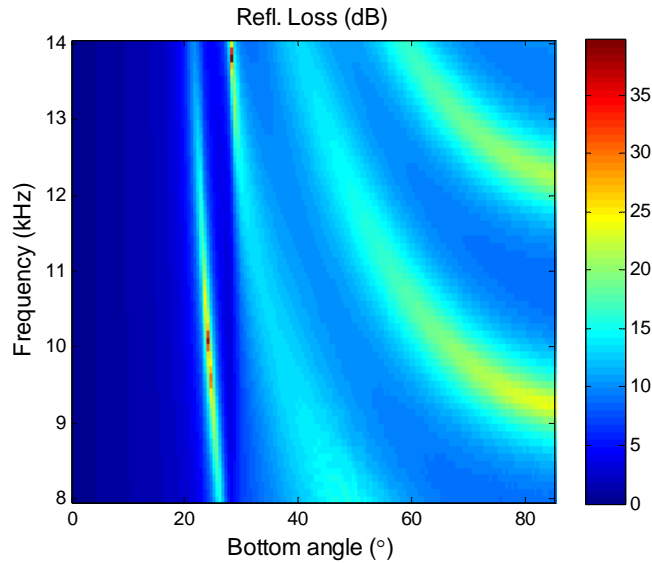
Figure 3.16: Modeled bottom reflection loss (two sediment layers).

24

Parameters	First layer	Second layer	Sub-bottom
Thickess	0.2	20	
$\rho(\text{g/cm}^3)$	1.5	2.1	2.1
$c_p(\text{m/s})$	1575	1700	2330
$\alpha_p(\text{dB/}\lambda)$	0.6	0.1	0.1
$cs(\text{m/s})$	67	700	1000
$\alpha_s(\text{dB/}\lambda)$	1.0	0.2	0.2

Table 3.1: Parameters set in acoustic model (two sediment layers).
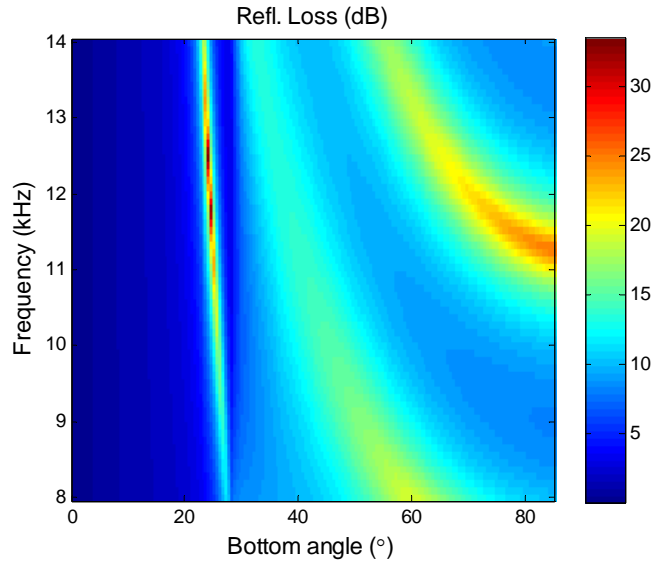
Figure 3.17: Modeled bottom reflection loss (one sediment layer).

Parameters	First layer	Sub-bottom
Thickess	0.175	
$\rho(\text{g/cm}^3)$	1.5	2.1
$c_p(\text{m/s})$	1575	1700
$\alpha_p(\text{dB/}\lambda)$	0.6	0.1
$cs(\text{m/s})$	0	700
$\alpha_s(\text{dB/}\lambda)$	0	0.2

Table 3.2: Parameters set in acoustic model (one sediment layer).

3.4   Conclusions

In this chapter, one simple geoacoustic inversion method based on bottom reflection coefficient (BRC) is investigated. It only needs to compare the downward and upward beam energy, comparing with that of an acoustic model. Since the vector array has the horizontal and vertical information, it can provide full spatial directivity. When the operating frequency is shifted to high frequency, using a small aperture VSA can invert some of the seabed

parameters. Otherwise, low frequency inversion methods should deploy a large vertical array to sample the depth-dependent mode information, or a long horizontal array to sample the time-disperse information.

The problem of the BRC inversion method is that the beam response is not ideal over a broadband of frequencies. Moving from the broadband to the endfire directions, the beams are broadened and this leads to an up/down ratio that does not produce a good estimate of reflection loss. This can be especially problematic at low grazing angles which is the part of the reflection loss curve that is often most important to estimate correctly. Techniques will be presented for mitigating the impact of beamwidth and grating lobes on estimating the seabed properties.

Chapter 4

Geo-parameter Sensitivity Analysis

Geo-parameter sensitivity analysis is to examine which of the seabed parameters are more sensitive to be estimated, when one parameter is varying among a specific range. So, sensitivity analysis is important in geoacoustic inversion, in order to improve the inversion efficiency. Some work can be found in [12]-[15]. It was demonstrated that, in most cases, the v_z-only processor achieves the highest resolution of the Barlett estimator. In [12], it was showed that the ($p+v$) and v_z-only processor are better than p-only processor with Makai sea trial data. In [13], the performance of using TRACEO ray model is simulated comparable with KRAKEN. In [14] and [15], also the Capon processor was studied, which showed much higher resolution than the Bartlett processor especially for compressional velocity, but the results fluctuates with time, and still has some ambiguity.

In this chapter, the main object is to investigate whether the knowledge of the vector field can improve the estimation performance of seabed parameters, comparing to that based only on the scalar pressure field.

There are a few measures to examine the parameter sensitivity in geoacoustic inversion. Bartlett estimator is used in this chapter, the Bartlett power is:

$$P_{Bart} = \frac{X_{rep}^{H}(X_{true}X_{true}^{H})X_{rep}}{N_{snaps} \parallel X_{rep} \parallel^{2}} \tag{4.1}$$

where X_{true} and X_{rep} are the true VSA data matrix and the replica vector, both are derived from the propagation model. And X can contain pressure-only data, vector-only data, or both of them, using the selection matrix proposed in 2.1.

4.1   Pekeris Waveguide

Figure 4.1 shows a simple Pekeris waveguide, in which an isovelocity water layer is over an isovelocity half-space bottom, and the seabed parameter is chosen as the Makai experiment [3], the sound velocity in the water is set as c_w=1500m/s.

ρ_w=1.0g/cm^3
c_w=1500m/s

z_s=98m

h=104m

ρ=1.5g/cm^3
c_p=1575m/s
α_p=0.6dB/λ
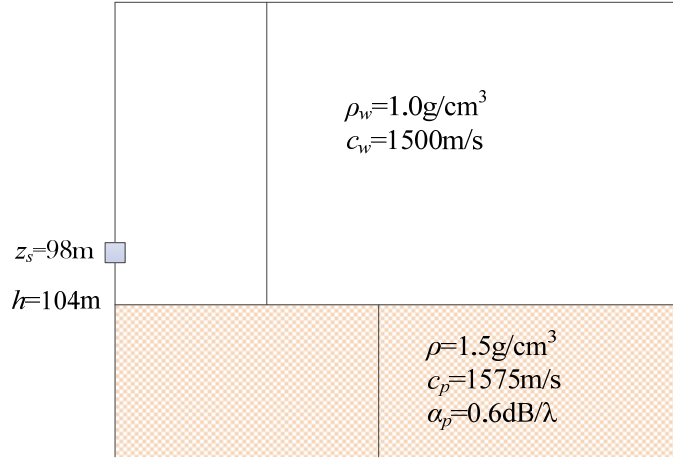
Figure 4.1: Schematic of the Pekeris waveguide.

4.1.1 Vector Signal Expressions

The pressure field and particle velocities of a harmonic source in a Pekeris waveguide can be approximated by the sum of trapped pressure and velocity modes. The pressure field is [16]:

$$p(r,z) = \sum_{m=1}^{M} A_m \Psi_m(z) H_0^{(1)}(k_m r) \tag{4.2}$$

where the time-dependent exponential component is omitted, Ψ is the depth-dependent pressure mode shape function. $H_i^{(1)}$ is the ith order Hankel function of the first kind. A_m is the mth mode amplitude.

The horizontal and vertical velocities are [16]:

$$v_r(r,z) = \sum_{m=1}^{M} \frac{-k_m}{j\omega\rho_0} A_m \Psi_m(z) H_1^{(1)}(k_m r) \tag{4.3}$$

$$v_z(r,z) = \sum_{m=1}^{M} \frac{1}{j\omega\rho_0} A_m \Phi_m(z) H_0^{(1)}(k_m r) \tag{4.4}$$

where Φ is the mode function for the vertical velocity, Ψ and Φ can be written as:

$$\Psi_m(z) = \sin\left[z\sqrt{k^2 - k_m^2}\right] \tag{4.5}$$

$$\Phi_m(z) = \sqrt{k^2 - k_m^2} \cos\left[z\sqrt{k^2 - k_m^2}\right] \tag{4.6}$$

and the mode amplitude is:

$$A_m = \frac{i2\pi P_s \Psi_m(z_s)}{h - \frac{\Psi_m(2h)}{2\sqrt{k^2 - k_m^2}} + \frac{\rho_w}{\rho_b}\frac{\Psi_m^2(h)}{\sqrt{k_m^2 - (\omega/c_b)^2}}} \tag{4.7}$$

where ρ_w and ρ_b are the densities of the water column and the seabed, and c_w and c_b are the

sound velocities in the water column and the seabed. P_s is the source pressure amplitude defined such that A_m has the dimension of pressure.

4.1.2   Simulation Results

Due to the much larger computational burden for higher frequency with normal mode model, the low frequency of 750Hz source signal is considered, and the number of sensors is N =4, sensor spacing is d=1m. Figure 4.2 shows the normalized Bartlett power versus the density, compressional velocity and compressional attenuation. It can be seen that, the resolution and sensitivity of v_z-only processor are worse than the other two, and the compressional velocity is more sensitive than the other two parameters.

Figure 4.3 gives the vertical beam power for a few VSA processing methods, the sidelobe level of v_z-only processor is the highest, and maximum response axis (MRA) is deviated from others.

(a)   (b)

(c)

Figure 4.2: Normalized Bartlett power vs. density (a), vs. compressional velocity (b) and vs. compressional attenuation (c). (f=750Hz, number of modes: 25).
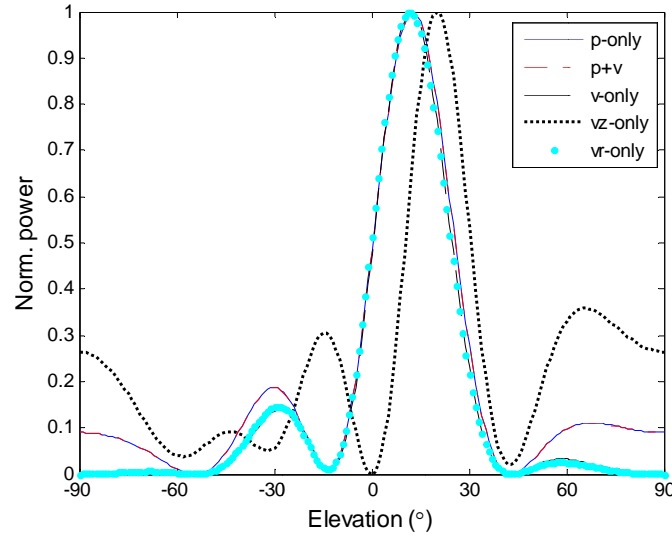
Figure 4.3: Comparison of vertical beams for Pekeris waveguide.

4.2 Makai Scenario

Figure 4.4 shows the Makai experimental scenario in Julian Day 264, since the high frequency geoacoustic inversion was considered in the VSA experiments, the seabed is considered as a half-space, and the shear was not considered here for it is not important in high frequency band. The source depth is 98m, and the depths of the four equispaced vector sensors are from 79.6 to 79.9m, the range is about 1830m.
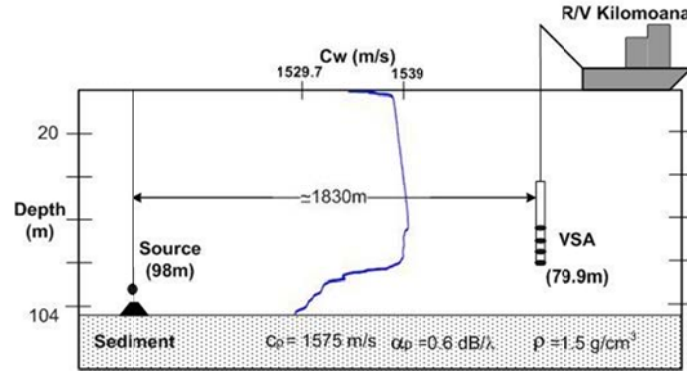
Figure 4.4: Makai experimental scenario.

4.2.1 Normal-mode Low Frequency Results

To use the normal-mode model, a scaled low frequency model is used to improve the computational efficiency, so the inter-element spacing is set as 1m, and the frequency is lowered to 750Hz.

With normal-mode model, the pressure and velocities can be written as [17]:

30

$$p(r,z) = j\sqrt{2\pi} \sum_{m=1}^{M} \frac{\Psi_m(z_s)\Psi_m(z)}{\rho(z_s)\sqrt{k_m r}} e^{jk_m r - j\pi/4} \tag{4.8}$$

where it is normalized such that the source level is 0dB at a reference range of 1m, and

$$v_r(r,z) = -\sqrt{2\pi} \sum_{m=1}^{M} \frac{k_m \Psi_m(z_s)\Psi_m(z)}{\rho(z_s)\sqrt{k_m r}} e^{jk_m r - j\pi/4} \tag{4.9}$$

$$v_z(r,z) = j\sqrt{2\pi} \sum_{m=1}^{M} \frac{\Psi_m(z_s)}{\rho(z_s)\sqrt{k_m r}} \cdot \frac{\partial \Psi_m(z)}{\partial z} e^{jk_m r - j\pi/4} \tag{4.10}$$

where the gradient of Ψ with respect to z is obtained by finite differential numerical method.

The KRAKEN package was used to compute the normal-mode signals [10]. Figure 4.5 shows the results of Bartlett estimators versus the density, compressional velocity and compressional attenuation. It can be seen that, using only four elements is difficult to estimate the seabed parameters. Figure 4.6 shows the corresponding vertical beam spectra. That the maximum of v_z beamforming deviates from others is due to the horizontal energy be suppressed, according to the beamforming weight vector.
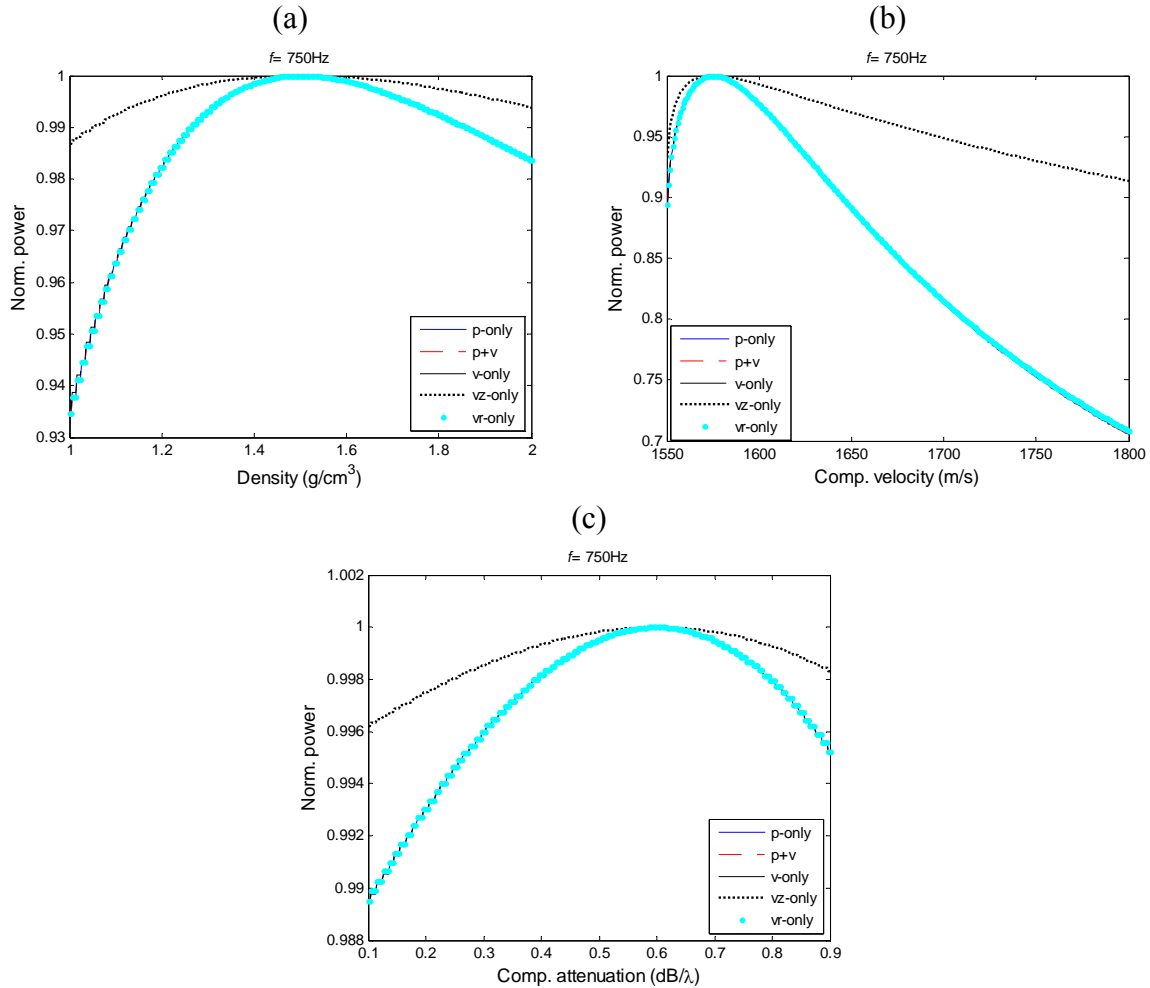

Figure 4.5: Normalized Bartlett power vs. density (a), vs. compressional velocity (b) and vs. compressional attenuation (c). (f=750Hz, Normal-mode model, number of modes: 12).

Figure 4.6: Vertical beams for Makai waveguide (Normal-mode model, N=4).

If the number of modes is not fixed when the parameter is varying, the performance of density and attenuation estimation can be improved, as in Figure 4.7, but the Bartlett spectrum of the compressional velocity is oscillated, so the result is not shown below.

(a)   (b)
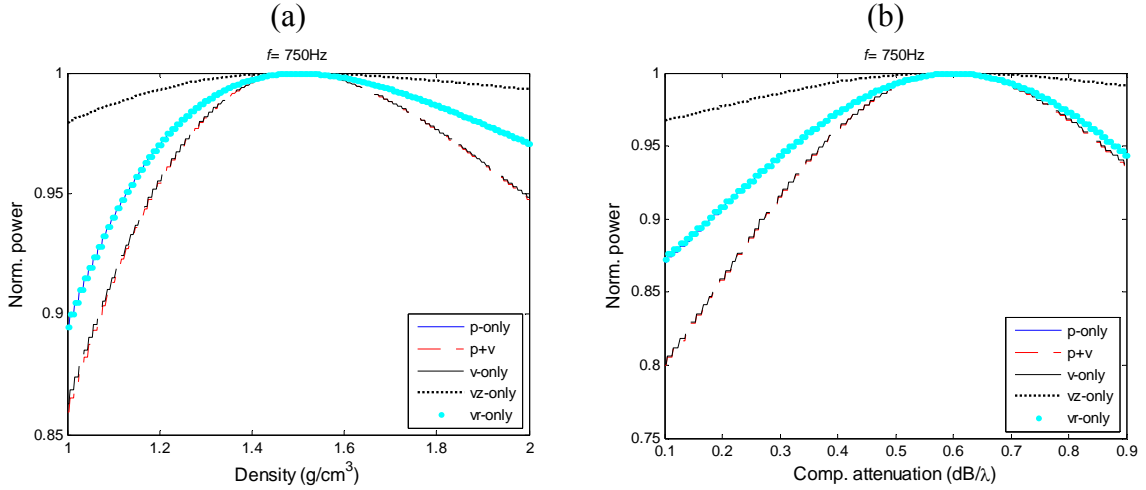
Figure 4.7: Normalized Bartlett power vs. density (a) and vs. compressional attenuation (b). (f=750Hz, all the modes are used).

4.2.2   16-element Normal-mode Low Frequency Results

In this section, the array aperture is enlarged to 15m with sensor depths ranging from 65m to 80m, i.e. *N*=15, *d*=1, and the number of modes is varying with the seabed parameter. Figure 4.8 shows the Bartlett results. Figure 4.9 is the normalized vertical beam power.

Figure 4.8 and Figure 4.9 show that the geoacoustic inversion performance is proportional to the array aperture. Figure 4.9 demonstrates that the sidelobe level is too high away from the broadside, when combining with the v_z component.
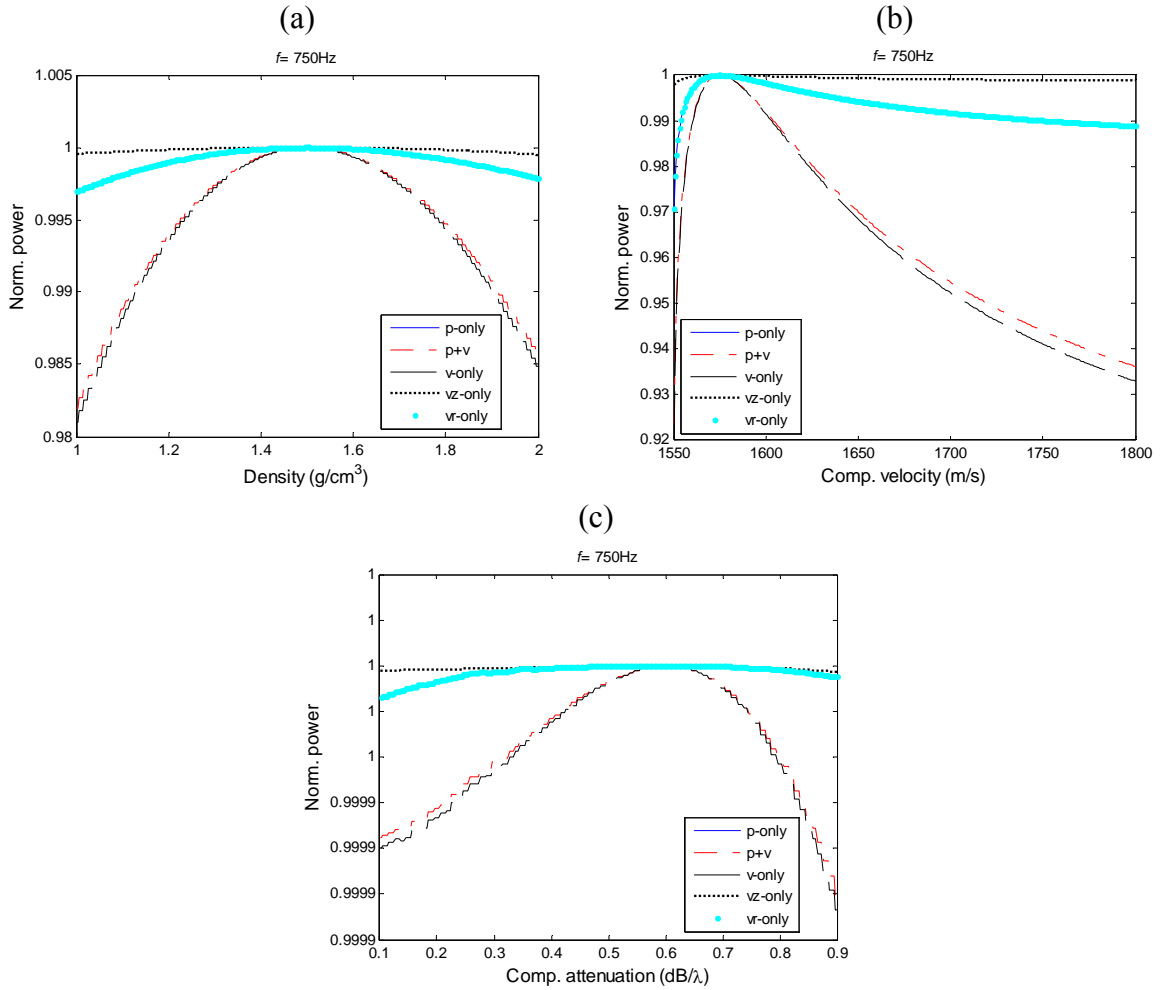
Figure 4.8: Normalized Bartlett power vs. density (a), vs. compressional velocity (b) and vs. compressional attenuation (c). (f=750Hz, N=16, Normal-mode model).
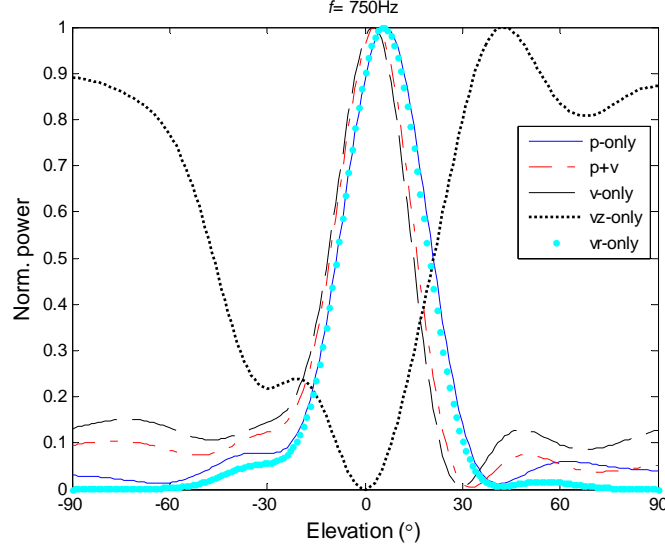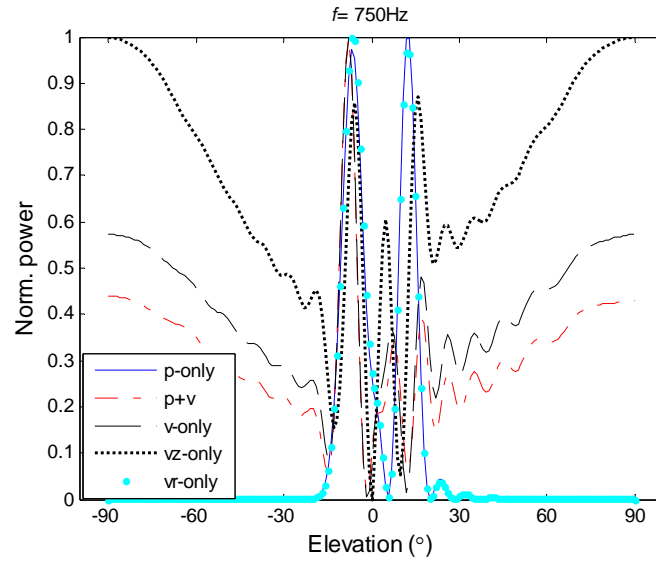

Figure 4.9: Vertical beams for Makai waveguide (Normal-mode model, N=16).

4.2.3 cTraceo Model Results

In this section, cTraceo model was used [2]. cTraceo is a Gaussian beam model developed in order to predict the acoustic pressure and particle velocities. Modeling particle velocity is important for vector sensor applications. cTraceo is especially useful for high frequency geoacoustic inversion. Also, cTraceo can include one or more targets in the waveguide, it can produce ray, eigenray, amplitude, and travel time information, even when the rays are reflected backwards on targets. cTraceo was benchmarked against tank data, demonstrating the reliability of the ray approach for seimo-acoustic applications [18].

Figure 4.10 and Figure 4.11 show the normalized Bartlett power versus the density, compressional velocity and compressional attenuation, for two frequencies: 13078Hz and 8250Hz. We can see that, the performance of higher frequency is better than that of lower frequency, and the performance of v_z-only processor in high frequency is the best. At low frequency, the 0.4m-aperture VSA is not sufficient to sample the vertical information. However, when running cTraceo, the v_z component is somewhat dependent on the number of launching beams with the maximum tracing beam angle is fixed. As a result, the performance of v_z-only processing fluctuates with the chosen tracing beam numbers.
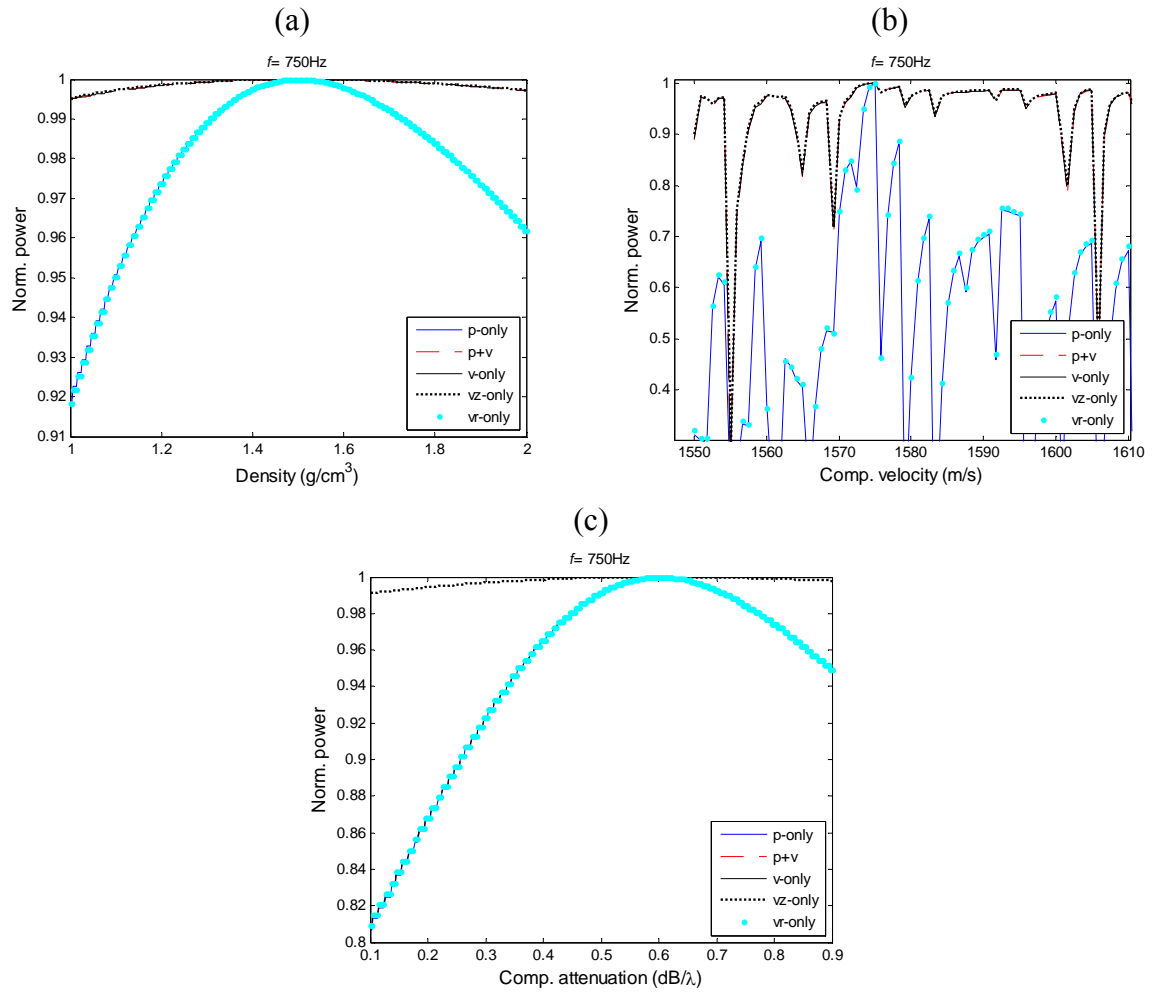
(a) (b)

(c)

Figure 4.10: Normalized Bartlett power vs. density (a), vs. compressional velocity (b) and vs. compressional attenuation (c). (f=13078Hz, cTraceo model).

Figure 4.11: Normalized Bartlett power vs. density (a), vs. compressional velocity (b) and vs. compressional attenuation (c). (f=8.25kHz, cTraceo model).

To see the influence of array aperture, the elements of *N*=4, 8, 16 are considered here with the deepest sensor depth be 79.6m. Figure 4.12 shows the corresponding Bartlett estimator results by using (*p+v*) processing. It can be seen that the resolution of geoacoustic parameters are decreasing with the array aperture increasing, it may be caused by the different incoming ray structures across the sensors at different depths.
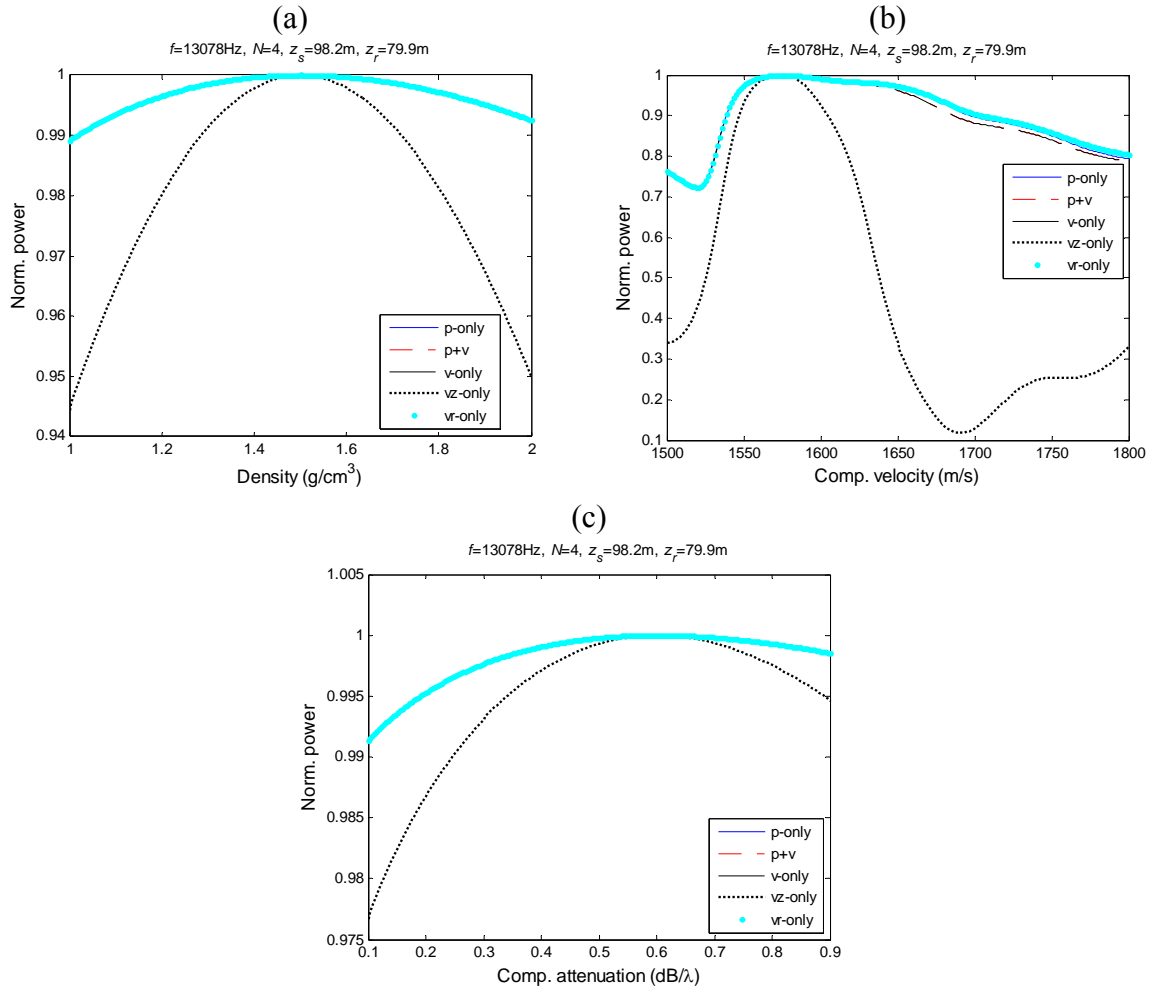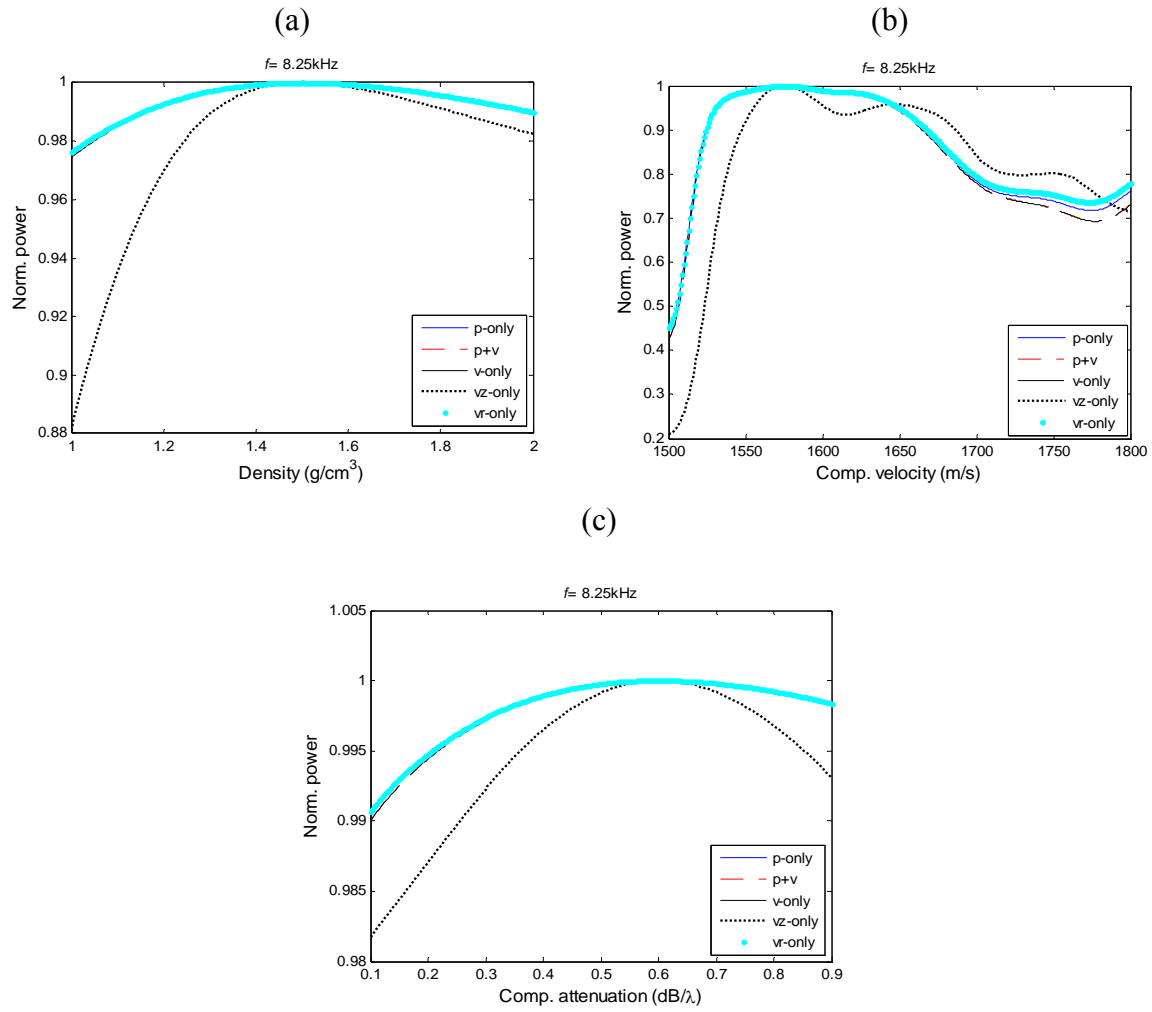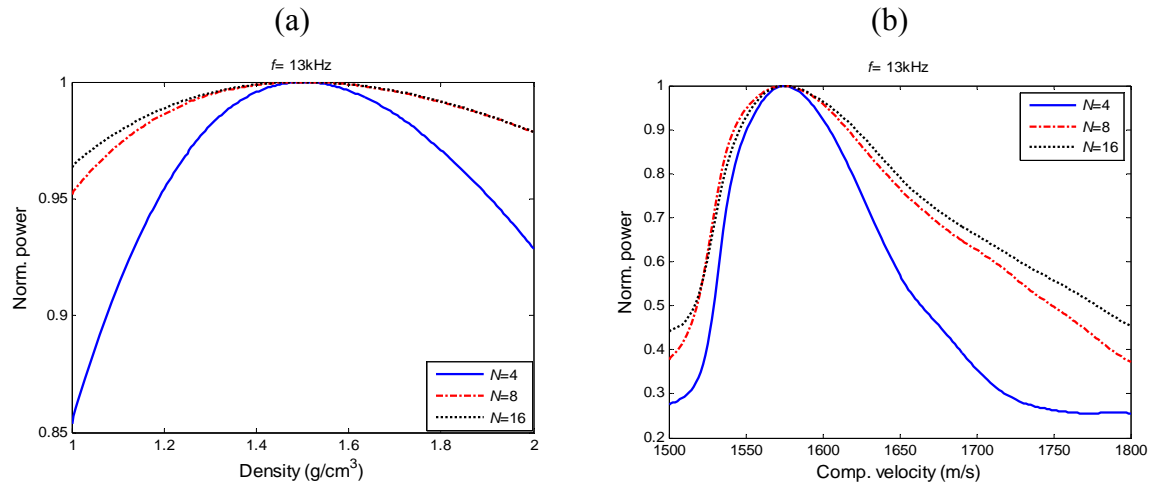
(c)

Figure 4.12: Normalized Bartlett power vs. density (a), vs. compressional velocity (b) and vs. compressional attenuation (c). (f=13kHz, (p+v) method, cTraceo model).

Figure 4.13 shows the Bartlett estimator results of different processing methods when the VSA elements is $N=16$. In this case, the v_z-only processor is a little better than others, but not significantly. So, by using cTraceo model, the 4-element VSA is enough for geoacoustic inversion, but the resolution is not satisfied, since the mainlobe of the Bartlett spectrum is wide, and it is almost impossible to estimate the density and attenuation (attenuation spectrum is not shown, therefore).

(a)   (b)
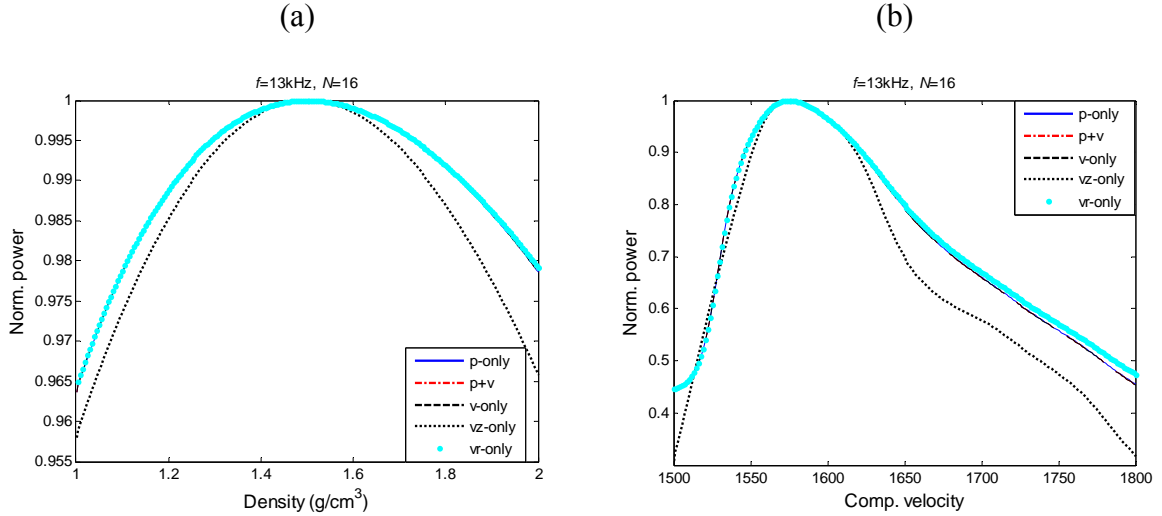
Figure 4.13: Normalized Bartlett power vs. density (a) and vs. compressional velocity (b) (f= 13kHz, N=16, cTraceo model).

4.2.4 MMPE Model Results

The Monterey-Miami parabolic equation (MMPE) model is a numerical model which can compute the particle velocity sound field [19]. It was based on the split-step Fourier (SSF) technique.

The time-harmonic acoustic field in a cylindrical coordinate system can be represented

as [19]:

$$P(r,z,\phi,\omega t) = p(r,z,\phi)e^{-j\omega t} \tag{4.11}$$

$$\frac{1}{r}\frac{\partial}{\partial r}\left(r\frac{\partial p}{\partial r}\right) + \frac{1}{r^2}\frac{\partial^2 p}{\partial \phi^2} + \frac{\partial^2 p}{\partial z^2} + k_0^2 n^2(r,z,\phi)p = -4\pi P_0 \delta(\bar{x}-\bar{x}_s) \tag{4.12}$$

where, k_0 is the reference wavenumber, $n(r,z,\phi)=c_0/c(r,z,\phi)$ is the acoustic refraction index. All features of the environment are represented within $c(r,z,\phi)$. The source is located $(0, z_s)$, and P_0 is the reference source level. And

$$\delta(\bar{x}) = -\frac{1}{2\pi r}\delta(z-z_s)\delta(r) \tag{4.13}$$

is a Dirc function defining the point source contribution.

The general form of the parabolic approximation to the Helmholtz wave equation for acoustic pressure can be defined as:

$$\frac{\partial \psi}{\partial r} = -ik_0(1-Q_{op})\psi = -ik_0 H_{op}\psi \tag{4.14}$$

Q_{op} is the pseudo-differential operator, H_{op} is a Hamiltonian-like operator which defines the evolution of the PE field function in range, and the PE field function ψ is defined as [19]:

$$p(r,z,\phi) = P_0\sqrt{\frac{R_0}{r}}Q_{op}^{-1/2}\psi(r,z,\phi)e^{jk_0 r} \tag{4.15}$$

The calculation of the velocity field will depend upon operations that are easily performed using Fourier transforms.

Figure 4.14 demonstrate the TL's of v_r and v_z components using MMPE model. The propagation in the seabed is included.
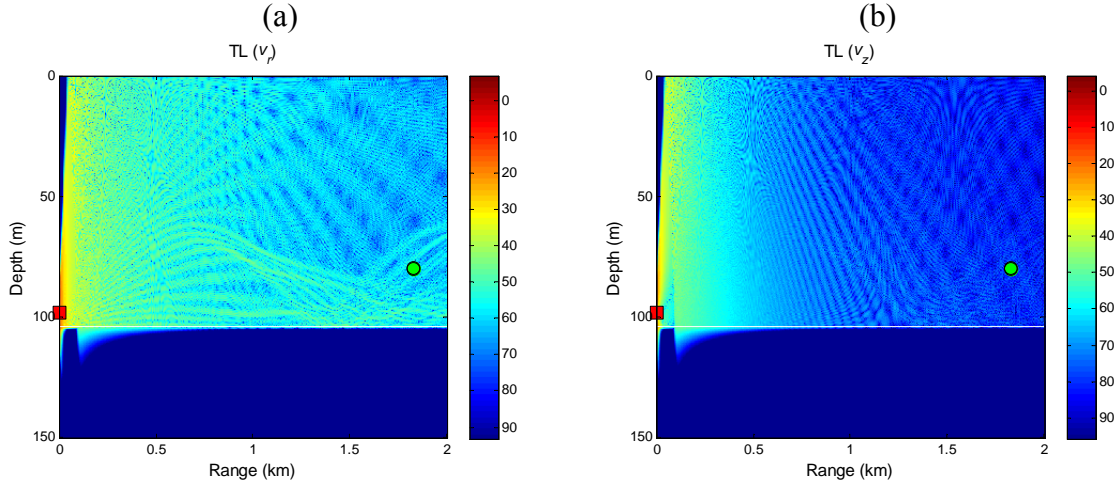
Figure 4.14: TL comparison between v_r (a) and v_z (b) using MMPE model (red square: source; green circle: receiver, f=13kHz).

Using MMPE model, the seabed parameter sensitivities of Bartlett estimator are shown in Figure 4.15. It can be seen that, only the compressional velocity can be estimated by MMPE model, and the resolution is lower than that of cTraceo.

(a)
(b)

(c)

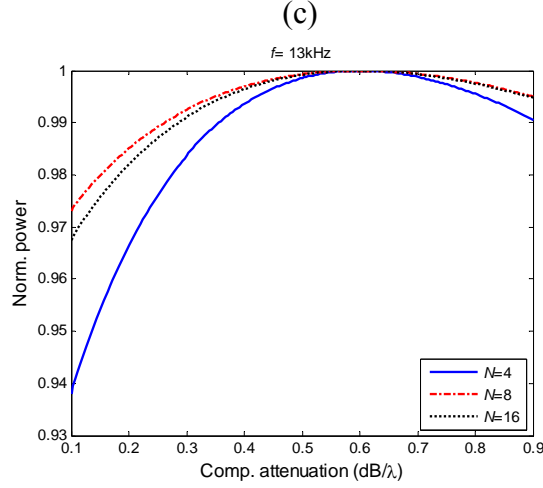*Figure 4.15: Normalized Bartlett power vs. density (a), vs. compressional velocity (b) and vs. compressional attenuation (c) (f=13kHz, MMPE model).*

4.2.5   Bellhop Model

For high frequency problems, the ray model provides results more rapidly. Even sometimes it is less accurate than other models, the inaccuracy can be neglected. Bellhop uses a robust variant of Gaussian beam tracing referred to as geometric beam tracing [10].

Figure 4.16 shows the TL's of the three components of p, v_r and v_z. Since p and v_r have the similar interference structures, see Figure 4.16 (a) and (b), and the sensitivity analysis also suggest that only the v_z-only processor is significantly different from other processors. So, when using the MFI algorithms, we only need to compare the inversion performance of the p-only processor and v_z-only processor, for sufficiently high SNR scenarios.

(a)

(b)

(c)
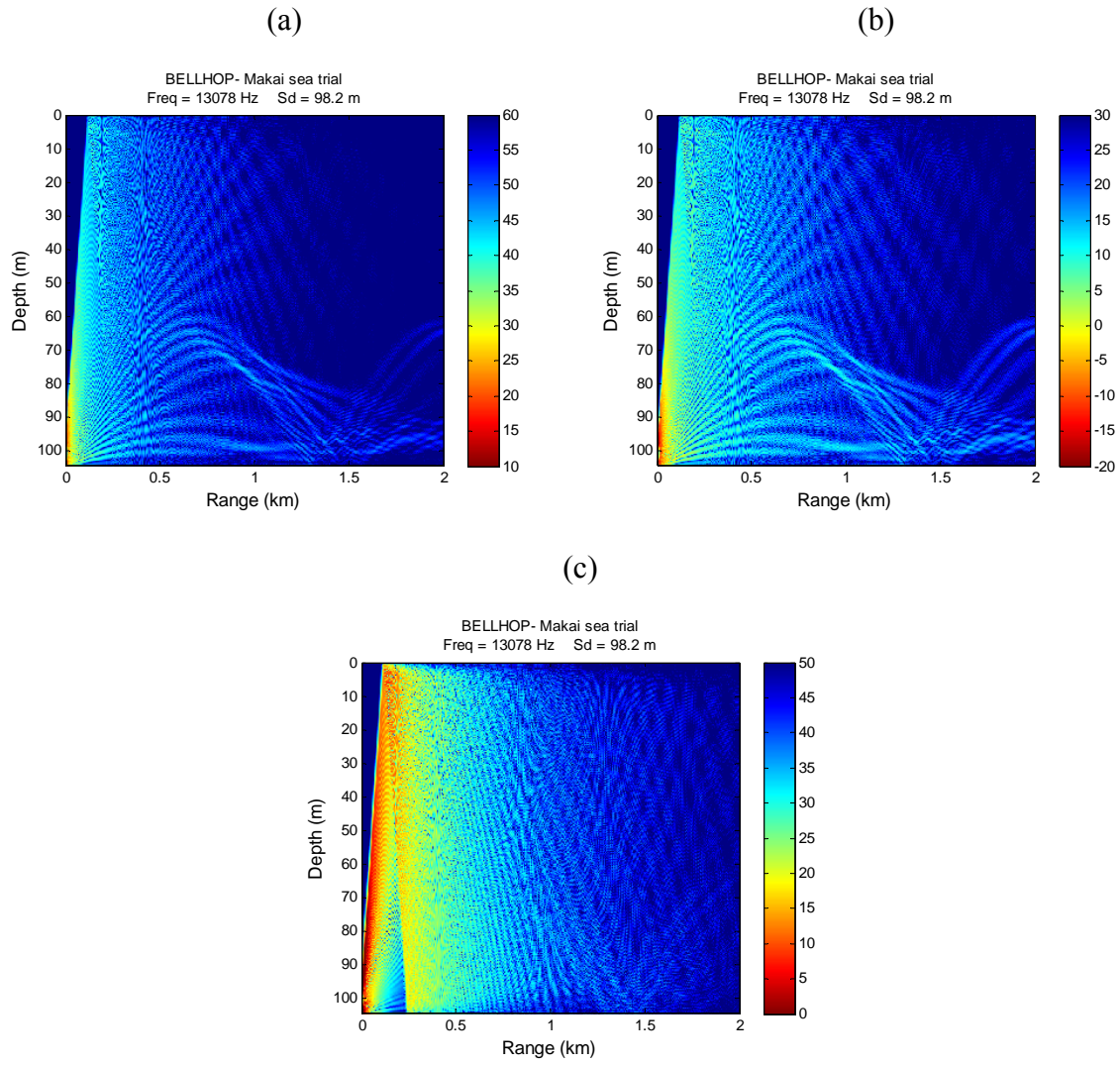
Figure 4.16: TL of p component (a), v_r component (b) and v_z component (c).

Figure 4.17 depicts the normalized Bartlett power vs. seabed parameters. It can be seen that the v_z-processor achieves the best performance, and the compressional velocity is the most sensitive parameter that can be inverted.

(a)

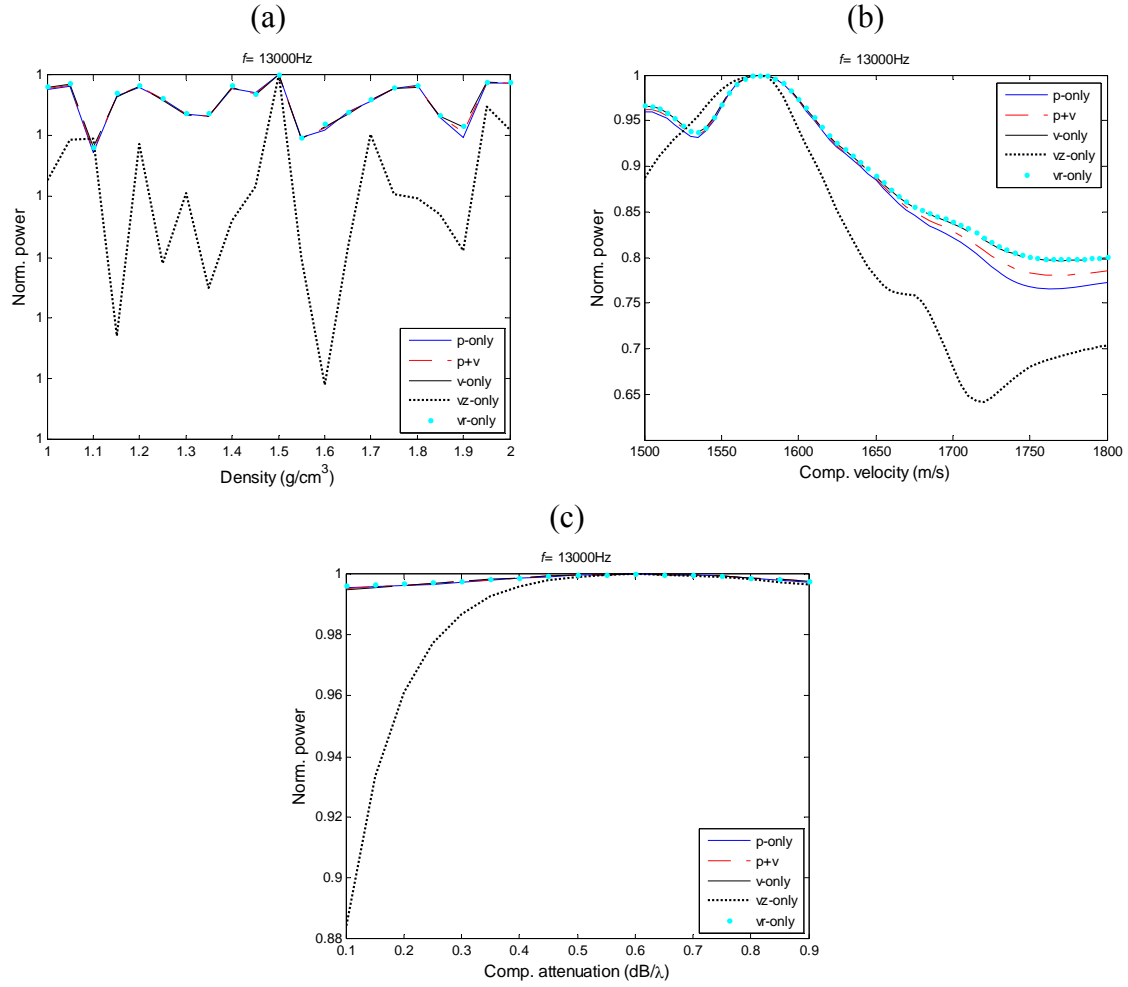(b)

(c)

f=13078Hz, *N*=4, r_s=1830m, z_s=98.2m, z_r=79.9m
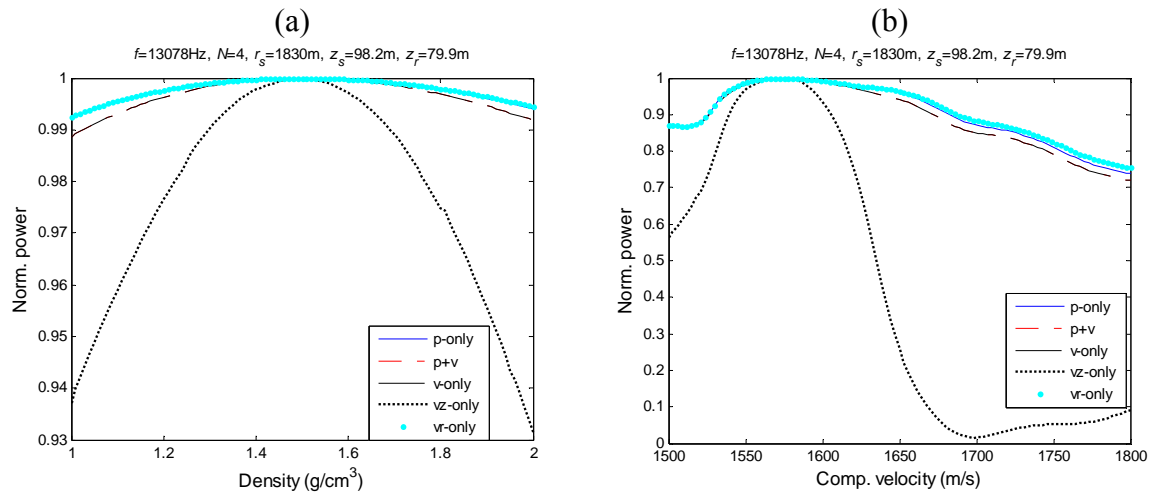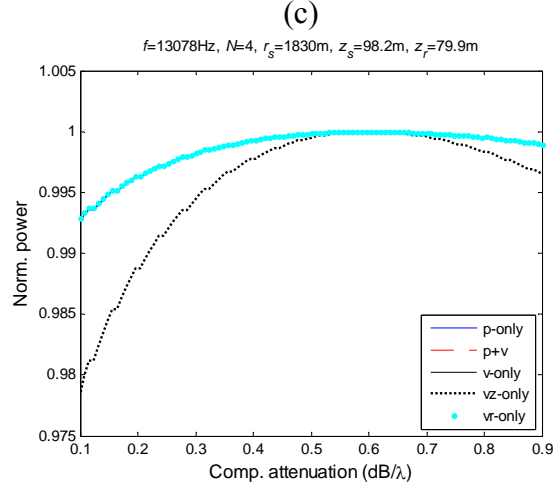
Figure 4.17: Normalized Bartlett power vs. density (a), vs. compressional velocity (b) and vs. compressional attenuation (c). (f=13078Hz,Bellhop model)

For different frequencies, the corresponding Bartlett normalized power are shown in Figure 4.18. The mainlobe at 13078Hz is narrower in the lower c_p area than the others, and the shape in the higher c_p area is similar to that by MMPE model, see Figure 4.15 (b). And to compare with the previous results of [3], the inversion techniques will be focused on frequency of 13078Hz.
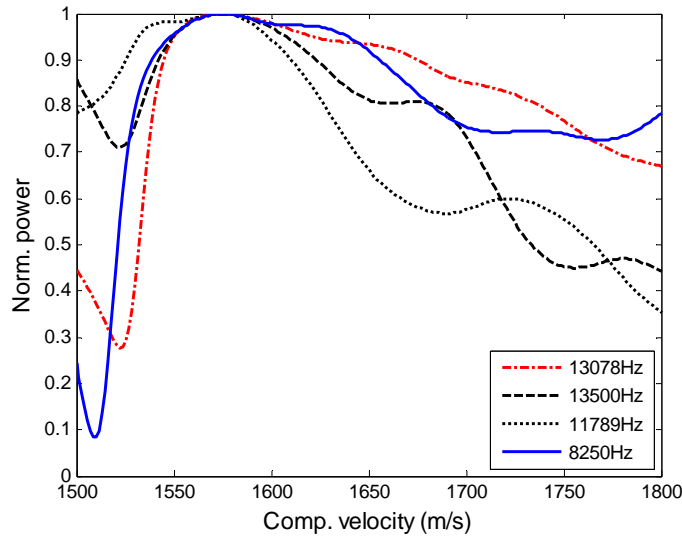
Figure 4.18: Normalized Bartlett power vs. c_p for different frequencies. (Bellhop ray tracing model).

4.3   Cramér-Rao Bound (CRB) Analysis

Geoacoustic parameters have a noticeable impact on the sound propagation, which is important to evaluate the sonar detection, tracking, localization, and communication performance, etc. Since the measured data undergo random fluctuations due to underwater

transmission media inhomogeneities and non-stationaries, these uncertainties often leads to nonlinear inverted estimates be biased and have large variance that may exceed the CRB by orders of magnitude.

CRB is the minimum attainable variance of any unbiased estimator. The mean-square error of any unbiased estimate of a deterministic parameter vector from random data cannot be less than the CRB, which exists given mild regularity conditions on the probability density of the data. This is true regardless of the method of estimation, and, for example, regardless of whether or not there are significant ambiguities, sometimes referred to as sidelobes in the estimation problem [20].

Parameter estimates are meaningful only if their errors fall within the design thresholds specified for the given experimental scenario. CRB is an extremely useful tool in aiding experimental design for geoacoustic inversion. The bounds of seabed parameter errors can be derived by running the propagation models to compute the theoretical CRB's. From which, if some parameters depart from the CRB's too much, it can be suggested that these parameters are not as sensitive as can be inverted. So, the multi-parameter inversion problem can be simplified to some extent, and one can focus on inversions of those more sensitive parameters, which are more probable to achieve the CRB's.

4.3.1 CRB Expression

Usually, the analytically closed expressions for CRB's are difficult or impractical to derive, depending on the assumptions.

It is well known that the CRB matrix is the inverse of the Fisher information matrix. For geoacoustic inversion, the emitted source is deterministic with its power unknown, and when the noise is assumed to be spatially and temporally zero-mean, circular, white Gaussian, then the deterministic Cramér-Rao Bound (CRB) of seabed parameter vector can be, similar to CRB's of bearing estimates, written as [4]:

$$\mathrm{CRB}(\boldsymbol{b}) = \frac{\sigma_n^2}{2N_{\mathrm{snaps}}} \left\{ \mathrm{Re}\left[(\boldsymbol{U} \otimes \boldsymbol{I}_q) \odot (\boldsymbol{D}^H \Pi_c \boldsymbol{D})^T \right] \right\}^{-1} \tag{4.16}$$

where $\boldsymbol{b}$ is the seabed parameter vector, and

$$\boldsymbol{U} = \sigma_s^4 (\sigma_s^2 \boldsymbol{a}^H \boldsymbol{a} + \sigma_n^2 \boldsymbol{I})^{-1} \boldsymbol{a}^H \boldsymbol{a} \tag{4.17}$$

$$\Pi_c = \boldsymbol{I} - \Pi \tag{4.18}$$

$$\Pi = \boldsymbol{a} (\boldsymbol{a}^H \boldsymbol{a})^{-1} \boldsymbol{a}^H \tag{4.19}$$

$$\boldsymbol{D} = \left[d_1 \cdots d_q \right], d_i = \partial \boldsymbol{a} / \partial b_i \tag{4.20}$$

where $\boldsymbol{a}$ is underwater channel Green's function, σ_s^2 and σ_n^2 are the signal and noise power, respectively. $\boldsymbol{D}$ is the derivative matrix, which is computed by numerical methods.

4.3.2 Numerical Results

Consider the Makai scenario in Julian Day 264, see Figure 4.4. The analysis frequency is 13078Hz. Using the Bellhop model, the CRB performance of density, compressional velocity and compressional attenuation is shown in Figure 4.19. The pressure was computed by geometric beam method, and the velocity components were by ray centered beams. It can be seen that, the performance of ($p+v$) is the best, since it has the maximum array gain. The v-only processing approaches the ($p+v$) processing with SNR increasing. Figure 4.20 shows the CRB performance by using cTraceo model. There is a little difference between Figure 4.19 and Figure 4.20, due to the different computational methods and accuracies. They both show that the ($p+v$) processing is the best, but in practical applications, the array calibrations are very important to combine the pressure and the particle velocity components. Later, the more precise model will be utilized to analyze the performance, and the influence of array calibration errors will be examined.

(a) (b)

(c)

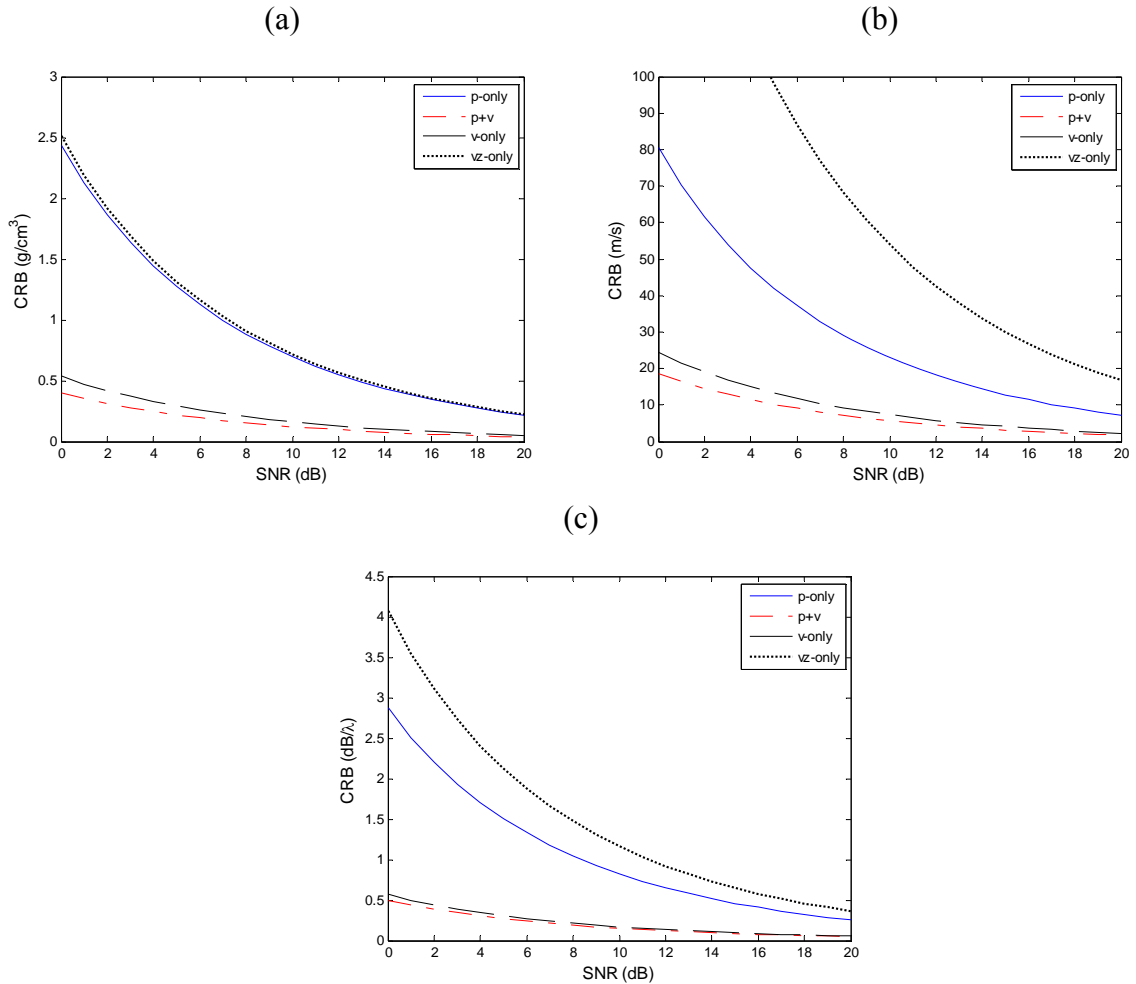*Figure 4.19: CRB of density (a), compressional velocity (b) and compressional attenuation (c) (f=13078Hz, Bellhop model).*

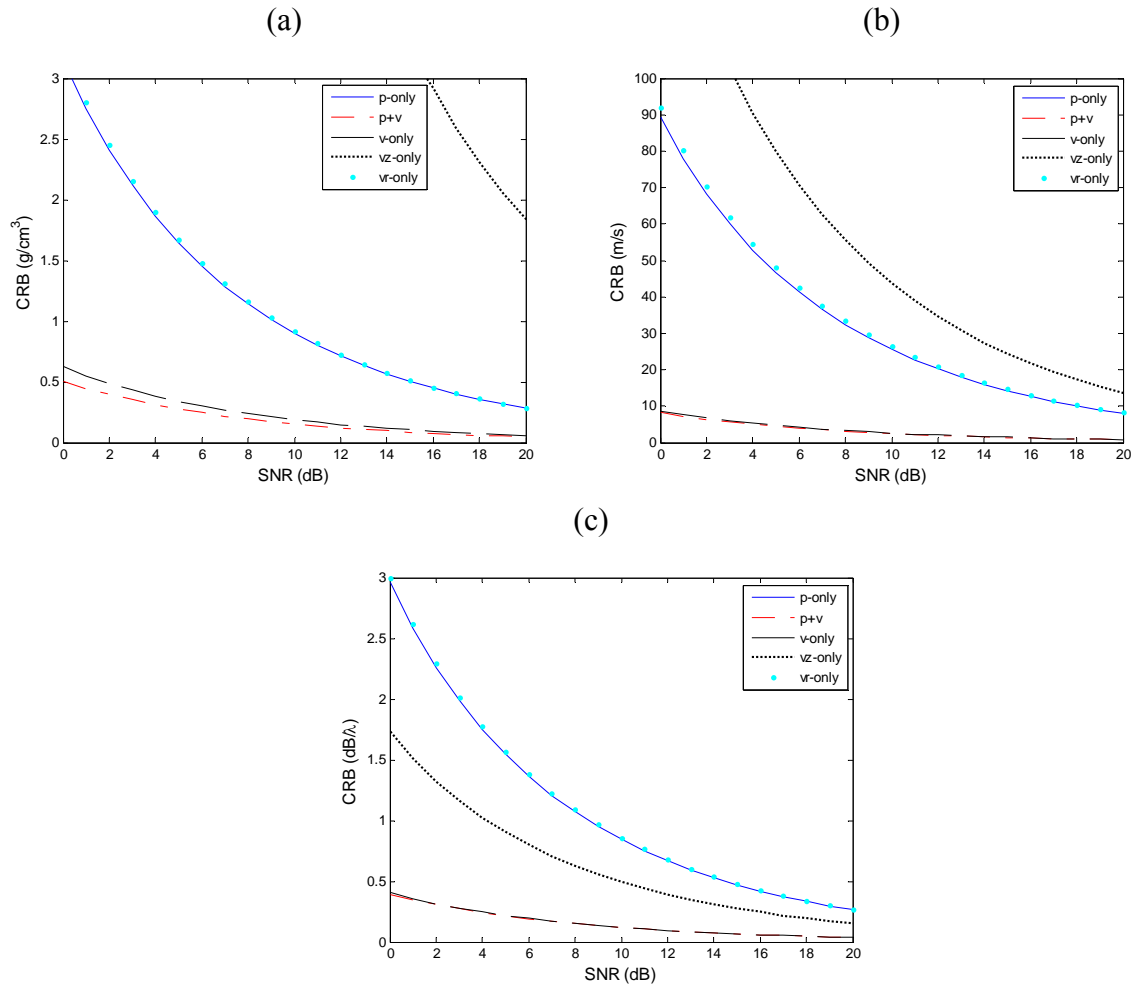*Figure 4.20: CRB of density (a), compressional velocity (b) and compressional attenuation (c) (f=13078Hz, cTraceo model).*

Chapter 5

Geoacoustic Inversion Using Global Optimization Method

There are a lot of parameters to be estimated in geoacoustic inversion, global optimization is an efficient approach without exhaustive searches. Among the mathematical optimization methods, genetic algorithm (GA) has attracted more and more attention in non-linear inversion problems. A comparison between GA and simulated annealing (SA) in underwater acoustics was presented in [21].

GA algorithms are analogous to biological evolution. The basic principle is: from all possible model signal vectors, an initial population of members is selected, the fit of each member is computed based on the fit between the observed data and the model data. Then through a set of evolutionary steps, the initial population evolves in order to become more fit. An evolutionary step consists of selecting a parental distribution from the population based on the individual's fit. The parents are then combined in pairs and crossover rate and mutation operators are applied to them to form a set of children. Finally, the children replace part of the population to increase the match between real data and simulated data. The detailed descriptions about GA algorithm and the performance measures can be found in [22], the SAGA software package. In this report, the MATLAB "ga" function was used, in order to integrate the cTraceo, UMPE (previous version of MMPE), and Bellhop models more conveniently. "ga" function also can provide a series of graphical functions to view the optimization process and performance. Some previous research results about using "ga" function on Makai'05 data processing can be found in [15].

Figure 5.1 shows the diagram of GA inversion.

The fitting function (cost function) is defined as

$$J = 1 - \frac{1}{N_f} \sum_{k=1}^{N_f} \frac{X_{rep}^H(f_k) R X_{rep}(f_k)}{\mathrm{tr}(R) \| X_{rep}(f_k) \|^2} \tag{5.1}$$

where X_{rep} is the replica signal, R is the correlation matrix from the observed data, N_f is the number of frequencies. $\| \bullet \|$ denotes the Frobenius norm, and $\mathrm{tr}(\cdot)$ the matrix trace.
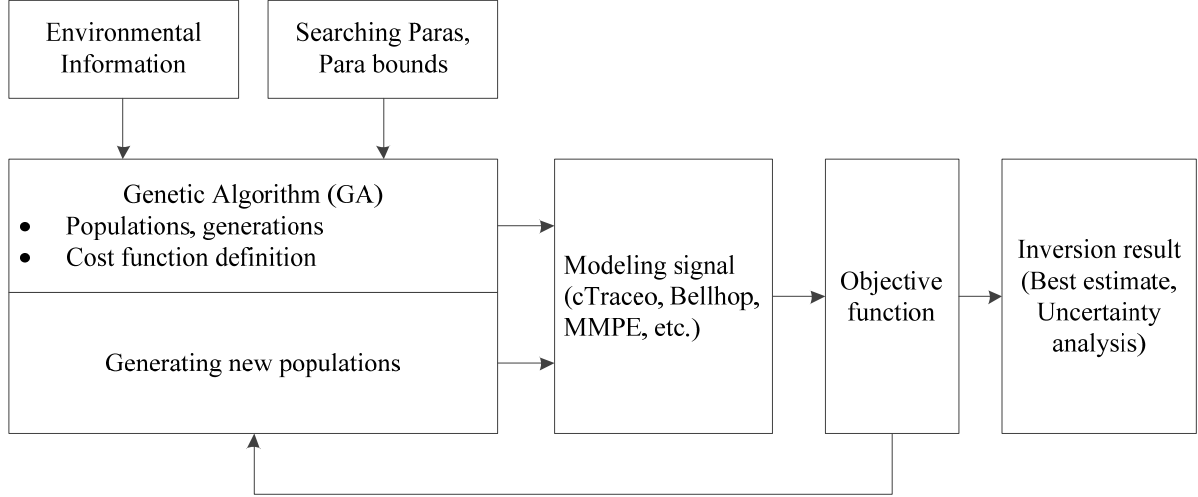
Figure 5.1: Diagram of GA inversion.

5.1 Simulation Results

Using cTraceo model, the true seabed values are: ρ=1.5g/cm^3, c_p=1575m/s, α_p=0.6dB/λ. Figure 5.2 shows the ($p+v$) geoacoustic inversion performance figures using the genetic algorithm. The parameter lower and upper bounds are [1.0g/cm^3, 1500m/s, 0.10dB/λ] and [2.0g/cm^3, 1800m/s, 0.90dB/λ], respectively. It demonstrates the effectiveness of the genetic algorithm used in vector sensor array geoacoustic inversion. Corresponding to Figure 5.2 (b), the estimated parameters are: $\hat{\rho}$ =1.4998g/cm^3, $\hat{c}_p$ =1579.7m/s, $\hat{\alpha}_p$ =0.617dB/λ.
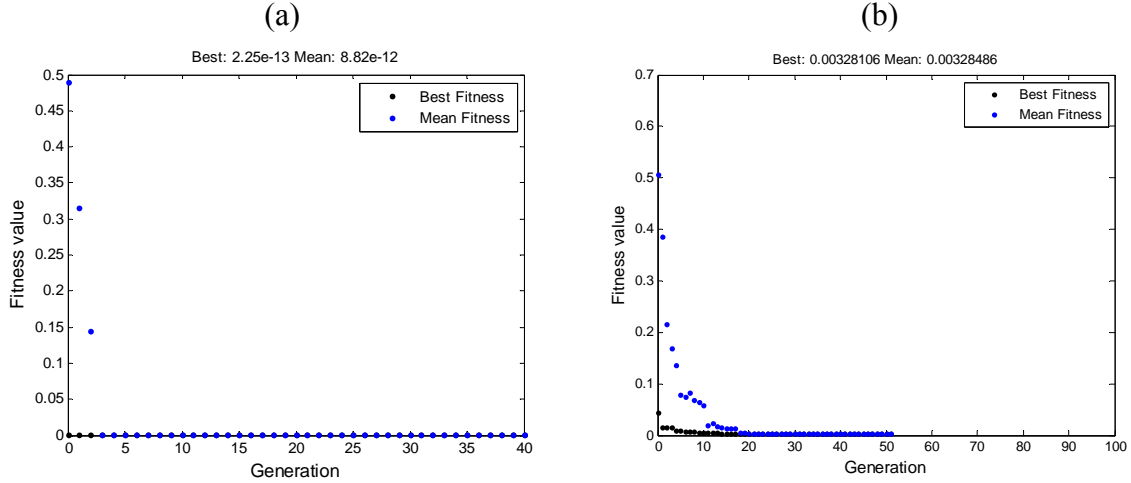
Figure 5.2: Fitness figures when only c_p is optimized with populations 5 and generations 40 (a) and three parameters are optimized with populations 15 and generations 51(b).

If averaged with multi-runs, the estimation accuracy could be improved further. Figure 5.3 shows the fitness and average distance between individuals of GA algorithm for the JD264 range-independent data, and the time at Min-3 was processed, ρ, c_p and α_p are optimized simultaneously. The mean fitness value is about 0.198, a little bigger under which

the satisfied result can be expected.

Figure 5.3: Fitness and average distance between individuals of GA processing.

5.2 c_p Inversion based on Bellhop Model
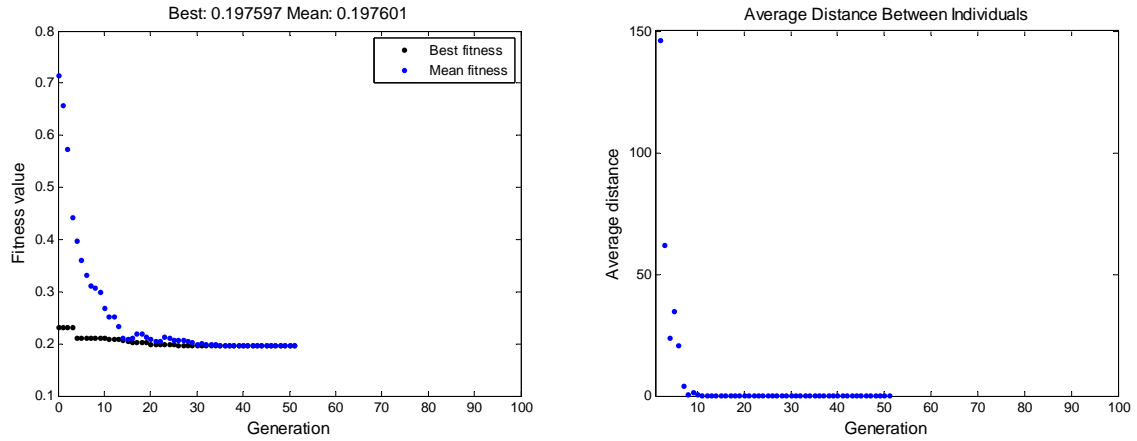
In this section, the JD264 data with duration up to 110 minutes are used to examine the inversion result stability, and the Bellhop model was used. Figure 5.4 shows the c_p-time-record (CpTR), the c_p can be tracked continuously. Figure 5.5 compares the c_p spectra of Bartlett and MVDR processing. The sidelobe can be greatly suppressed by MVDR, but the mainlobe fluctuates slightly with time, due to the high resolution characteristic of MVDR estimator, as indicated in Figure 5.5.
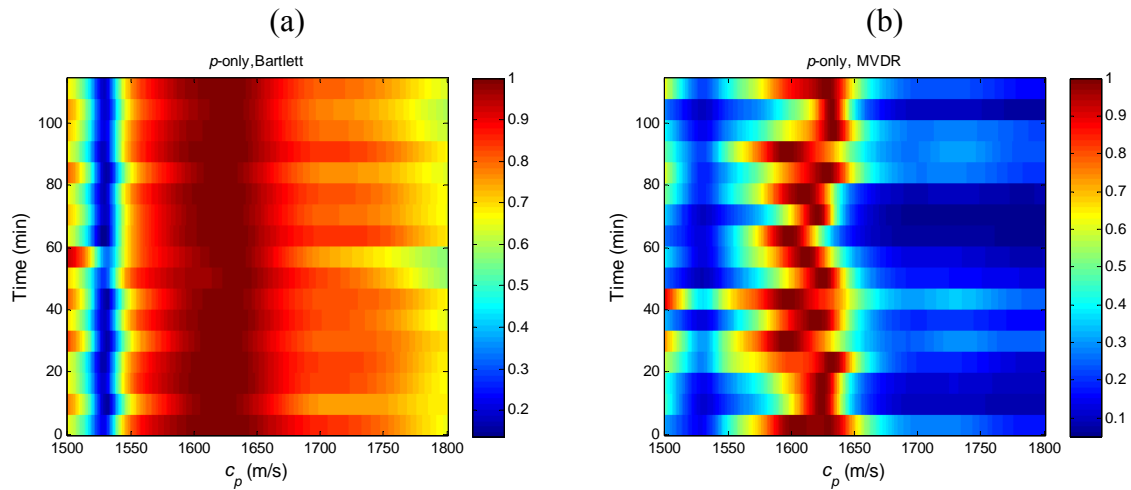
(a)   (b)

Figure 5.4: c_p inversion results of Bartlett estimator (a) and MVDR estimator (b).
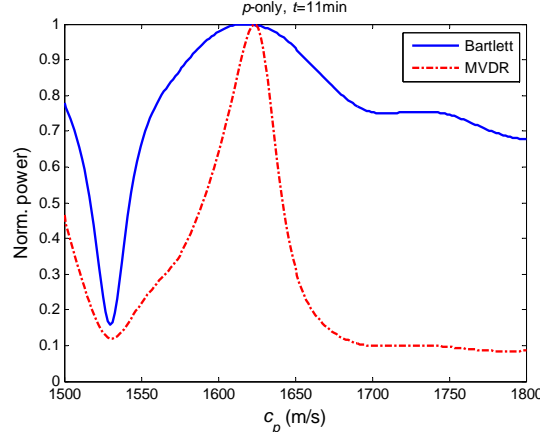*(f=13078Hz, p-only processing, JD264 data).*

Figure 5.5: Comparison of c_p spectra with Bartlett and MVDR processing.

Since the range and depth of the VSA may have errors, the inversion process is in two steps, demonstrated in Figure 5.6. First, three parameters: c_p, r, z_r (depth of the deepest sensor) are optimized by GA module, and the parameter lower and upper bounds are set as [1500m/s, 1.78km, 78.9m] and [1770m/s, 1.92km, 80.9m]. The resulting estimates of $\hat{r}$ and $\hat{z}_r$ are 1.9km and 79.3m, respectively. Then, replace with these two new geometrical parameters to generate the replica signals, after matching with the observed data, the c_p-time-record (CpTR) and the c_p spectra are shown in Figure 5.7 and Figure 5.8. It can be seen that, the resolution and estimation accuracy of c_p are improved significantly, which is around 1575m/s, in consistent well with the previous research results of the project SENSOCEAN [3]. Figure 5.8 also suggests that MVDR processing is promising in geoacoustic inversion.
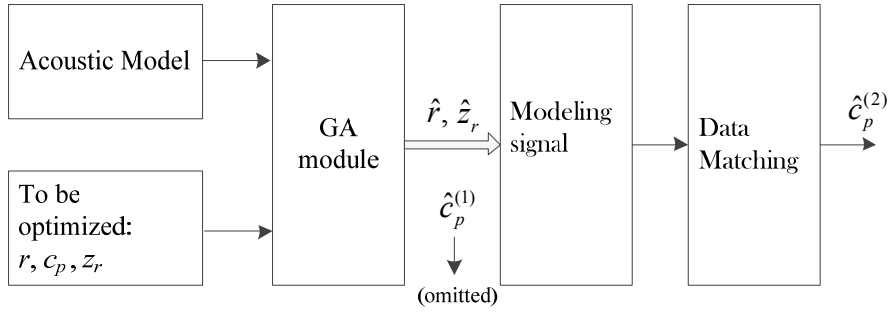

Figure 5.6: Block diagram of the proposed two-step inversion method.

47

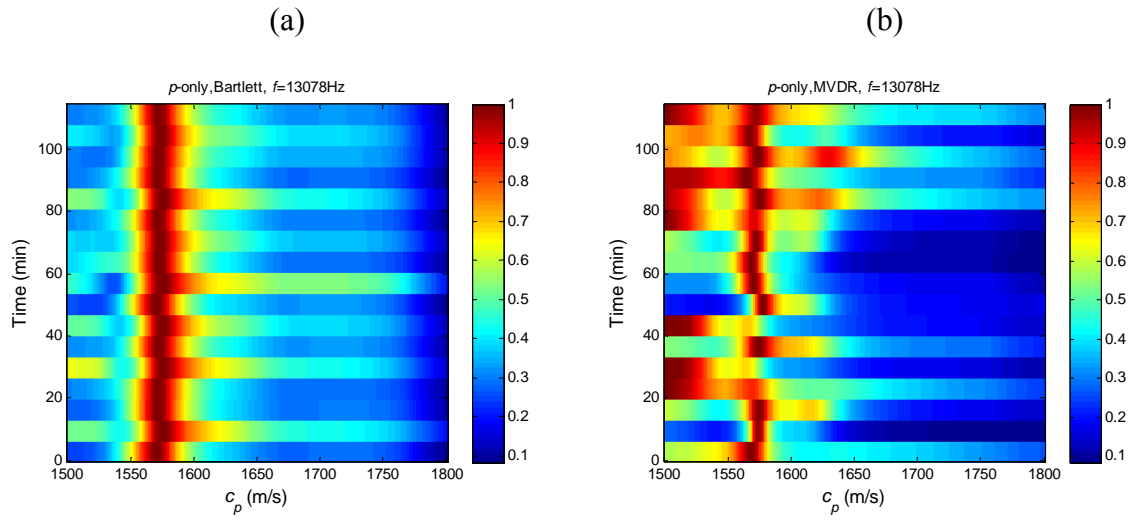*Figure 5.7: c_p inversion results after GA optimization: Bartlett estimator (a) and MVDR estimator (b) (f=13078Hz, p-only processing, JD264 data).*

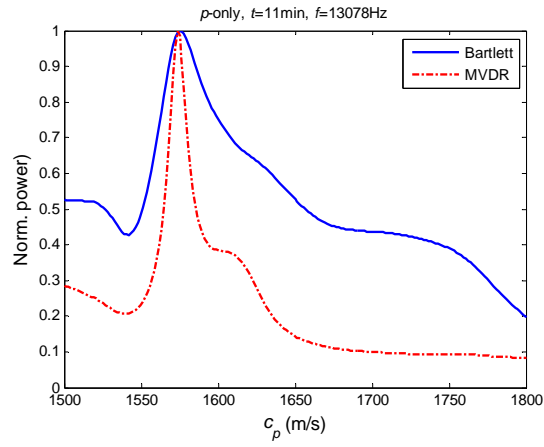*Figure 5.8: Comparison of c_p spectra with Bartlett and MVDR processing, after GA optimization.*

Chapter 6

Conclusion and Future Work

When sound interacts with the seafloor, the structure of the ocean bottom becomes important. Geoacoustic inversion provides a more efficient way to characterize the bottom than other oceanic measuring means. In order to reduce the system complexity, high frequency geoacoustic inversion methods were investigated in the SENSOCEAN project. In this report, some further research works were performed. The vector sensor array (VSA) signal processing methods and performance were summarized. The bottom reflection coefficient (BRC) inversion method was derived by ray model, and from the data processing results, it was concluded that the VSA has advantage in using this method, due to the vertical velocity field utilized. More results about the seabed parameter sensitivity of Bartlett estimator are presented, using different acoustic models, and low frequency inversion performance was investigated also. Cramér-Rao bounds (CRB's) of seabed parameters were analyzed, which also demonstrate the attractive advantage of VSA in geoacoustic inversion. Finally, genetic optimization inversion method was developed. Considering the performance of high frequency inversion is sensitive to the geometrical configurations, a two-step inversion method was proposed, that the receiver range and depth are optimized using GA algorithm, followed by matched field inversion, the resulting c_P-time-record (CpTR) performance was significantly improved.

The future work might involve as follows, theoretical analysis on how to set the optimal frequency, source-receiver configuration and algorithms in VSA geoacoustic inversion, simulations and performance analyses of BRC inversion method, and to improve the sea trial data processing results.

Bibliography

[1] P. Santos, *Vector sensor array data report: Makai Ex 2005*. Internal Rep 01/08 – SiPLAB/CINTAL, Univ. of Algarve, Faro, Portugal, Mar, 2008.

[2] O. C. Rodríguez, *The TRACE and TRACEO ray tracing programs*. http://www.siplab.fct.ualg.pt/models.shtml.

[3] P. Santos, *Ocean parameter estimation with high-frequency signals using a vector sensor array*. Ph.D thesis, Univ. of Algarve, 2012.

[4] A. Nehorai and E. Paldi, "Acoustic vector-sensor array processing," *IEEE Trans. Signal Process.*, vol. 42, pp. 2481-2491, Sep. 1994.

[5] M. Hawkes, A. Nehorai, "Acoustic vector-sensor beamforming and Capon direction processing," *IEEE Trans. Signal Process.*, vol. 42, pp. 2291-2304, Sep. 1998.

[6] R. J. Urick, *Principles of Underwater Sound, 3rd Edition*. McGraw-Hill, 1983.

[7] B. A. Cray and A. H. Nuttall, "Directivity factors for linear arrays of velocity sensors," *J. Acoust. Soc. Am.*, vol. 110, no.1, pp. 324-331, Jul. 2001.

[8] C. H. Harrison and D. G. Simons, "Geoacoustic inversion of ambient noise: A simple method," *J. Acoust. Soc. Am.*, vol. 112, no. 4, pp. 1377-1387, Oct. 2002.

[9] M. Siderius and C. H. Harrison, "High-frequency geoacoustic inversion of ambient noise data using short arrays", *AIP Conference Proc. 728*, pp. 22-31, 2004.

[10] M. B. Porter, *The KRAKEN normal mode program.* Tech. Report, SACLANT Undersea Research Centre, La Spezia, Italy, 1991.

[11] H. Schmidt, *OASES version 3.1 User guide and reference manual*, MIT, 2004.

[12] P. Santos, O. C. Rodríguez, P. Felisberto, S. M. Jesus, "Seabed geoacoustic characterization with a vector sensor array," *J. Acoust. Soc. Am.*, vol. 128, no.5, pp.2652-2663, Nov. 2010.

[13] O. C. Rodríguez, P. Felisberto, et. al, "Vector sensor geoacoustic estimation with standard arrays," in *Proc. 11th EUCA*, 2009.

[14] P. Felisberto, et. al, "Comparing the resolution of Bartlett and MVDR estimators for bottom parameter estimation using pressure and vector sensor short array data," in *Proc. Oceans'13*, Jun. 2013.

[15] J. D. Schneiderwind, *Geoacoustic inversion applied to the Makai JD264 and JD267*

data. Internal Rep 01/12 –SiPLAB/CINTAL, Univ. of Algarve, Faro, Portugal, Mar, 2012.

[16] D. R. D'Osto, P. H. Dahl and J.-W. Choi, "Properties of the acoustic intensity vector field in a shallow water waveguide," *J. Acoust. Soc. Am.*, vol. 131, no.3, pp. 2023-2035, Mar. 2012.

[17] F. B. Jensen, W. A. Kuperman, M. B. Porter and H. Schimdt, *Computational ocean acoustics*. New York: AIP press, 1994.

[18] O. C. Rodríguez, et. al, "Seismo-acoustic ray model benchmarking against experimental tank data," *J. Acoust. Soc. Am.*, vol. 132, no.2, pp.709-717, Aug. 2012.

[19] K. B. Smith, "Convergence, stability, and variability of shallow water acoustic predictions using a split-step Fourier parabolic equation model," *J. of Comp. Acoust.*, vol. 9, pp. 243-285, 2001.

[20] M. Zanolin, I. Ingram and et. al. "Asymptotic accuracy of geoacoustic inversions," *J. Acoust. Soc. Am.*, vol. 116, no.4, Pt.1, pp. 2031-2042, Oct. 2004.

[21] P. Gerstoft and Z.-H. Michalopoulou, "Global Optimization in Matched-Field Inversion," in *Proc. 4th European Conf. on underwater acoustics*, pp. 27–32, Rome, 1998.

[22] P. Gerstoft, *SAGA User Manual 5.4: An inversion software package*. UCSD: MPL, Sep. 2007.